PANA-GOESP-CR2

GOES D, E, F PROGRESS REPORT

ENERGETIC PARTICLE SENSOR TELESCOPE CALIBRATION WORK

Analysis Report
P. O. #T8-779416-LY5

Calibration Report
P. O. #08-779413-LBG
November 16, 1979

Prepared for

Hughes Aircraft Company
P. O. Box 92919
Los Angeles, CA 90009

by

PANAMETRICS, INC.
221 Crescent Street
Waltham, MA 02154

(This report is intended only for internal management use of Panametrics, Inc. and Hughes Aircraft Company.)

TABLE OF CONTENTS

LIST OF ILLUSTRATIONS

LIST OF ILLUSTRATIONS (Cont'd)

LIST OF ILLUSTRATIONS (Cont' d)

****

LIST OF TABLES

1. INTRODUCTION

1.1 Overview

This report provides a summary of the geometrical factor results for the GOES D, E & F Energetic Particle Sensor (EPS) Telescope. This unit measures protons and alpha particles from approximately 1 to 20 MeV/nucleon. Because GOES is a geosynchronous orbit satellite, the particle flux consists essentially of that from solar proton events (in which the alpha particle intensity is generally a few percent of the proton intensity), superimposed upon a lower level of outer radiation belt trapped protons having insignificant intensity above a few MeV. Although this Telescope unit is similar to that used on the previous GOES and SMS satellites, it is different in some significant design details. It was, therefore, decided that a program of engineering model calibration using particle accelerators would be carried out in order to determine the variation of geometrical factors (i.e., the detection efficiency) with incident particle energy and angle for both protons and alpha particles.

There are two types of geometrical factors of interest: that for the in-aperture particles in the relatively low energy range to be measured, and that for the high energy particles (essentially protons) that are capable of penetrating the Telescope shielding and producing spurious counts.

The "low energy" measurements were made at Brookhaven National Laboratory on the Tandem Van de Graaff facility, which provided protons to more than 30 MeV (three-stage) and alpha particles to more than 40 MeV (two-stage). The high energy work was done at the Harvard Cyclotron, which provides a fixed energy ~160 MeV proton beam. The particle energy could be decreased by absorbers, after exit from the cyclotron, in order to obtain data down to the lowest energy capable of penetrating the out-of-aperture shielding.

This first section of the report contains a brief design description, including a listing of the energy bins, and a summary of the accelerator data-taking operations. The second section of the report is devoted to the primary geometrical factor determinations, while the third gives details of spurious count results due to penetrating protons. The fourth section contains a brief summary of all results and some conclusions. Acknowledgements conclude the report.

1.2 Design Description

A cross section of the (basically) cylindrical Telescope Detector is shown in Figure 1.1. Essentially, it consists of front and back surface barrier detectors, approximately 50 μm and 500 μm in thickness, respectively, with necessary shielding. The geometrical factor is defined by two Super Densalloy (tungsten alloy) shields: the Front Collimator and the Shield. There is a 0.145 mil aluminum foil as a Light Shield, and a Magnet (not cylindrical) that eliminates potential pile-up effects due to low energy electrons ($\lesssim 50$ keV). The geometry is such that any particle that can pass through the cylindrical hole in the Shield must pass through the main body of the detector (s), well removed from their periphery. This minimizes the possibility of abnormally small energy losses being produced

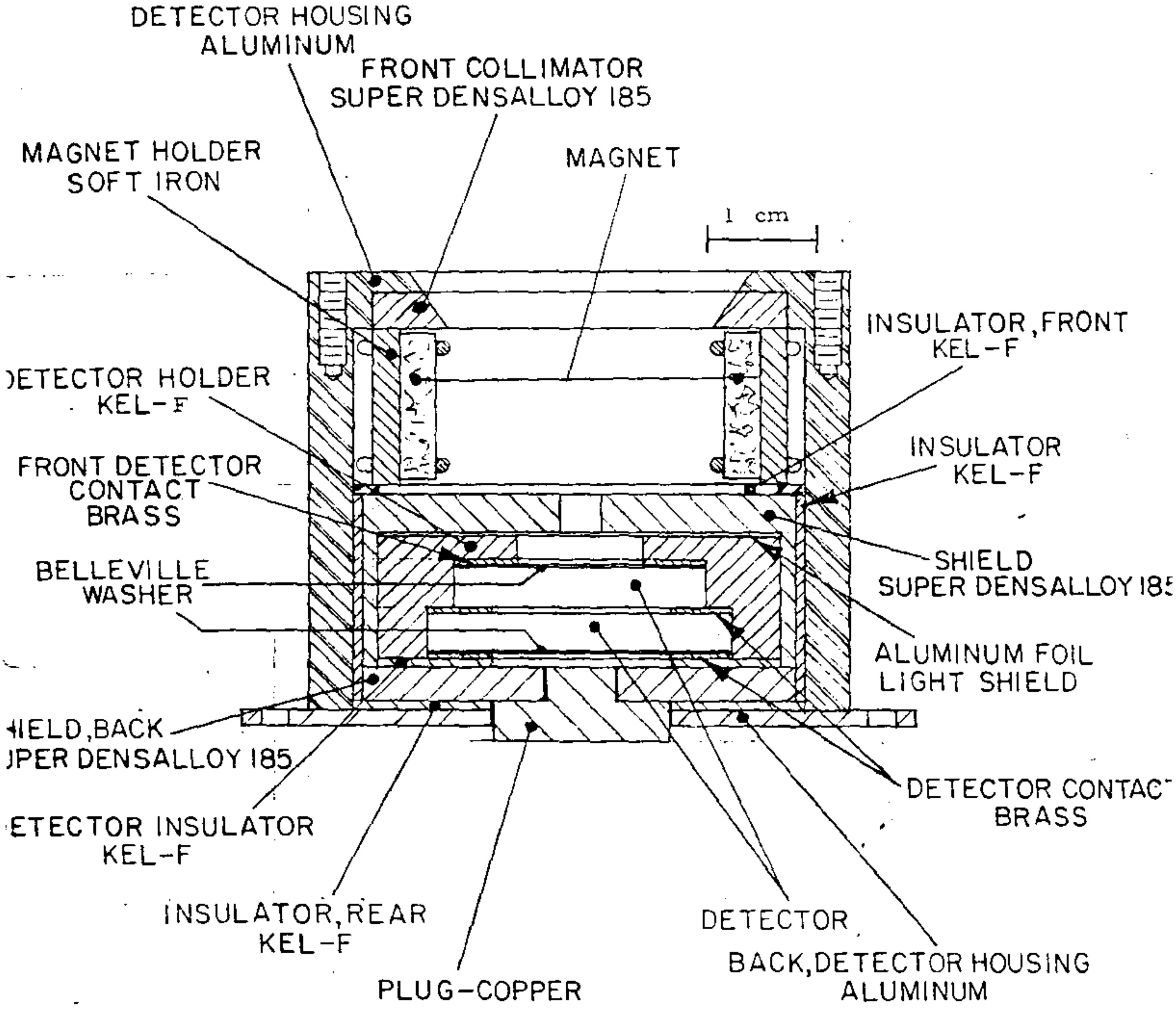

Fig. 1.1

TELESCOPE DETECTOR CROSS SECTION

by particles passing just through the detector edges. The various particle/ energy bins are formed by coincidence/anti-coincidence logic on the pulses produced by passage of a particle through the detector(s).

1.3 Energy Bin Definition

In order to define the energy/particle bins, it is necessary to calculate energy losses in the foil and the two detectors for the types of particles of interest. Here we use the following expression for the stopping power:

$$S(E) = -dE/ds = \left(\frac{1}{kn}\right)(E + \epsilon)^{1-n} \tag{1.1}$$

This is similar to the simple power law expression often used to approximate the stopping power, except that the constant ϵ is included. This causes S(E) to approach a constant, rather than infinity, as $E \longrightarrow 0$. Experimentally, it is found that S(E) peaks at a very low energy (~ 100 keV), but this is unimportant for present purposes because the range of protons and alphas $\lesssim 100$ keV is small ($\lesssim 1 \mu$m Si).

By use of (1.1), it is simple to show that the average energy just necessary to pass through a pathlength s of any absorbing material, the so-called "range energy", is

$$E_r = (\epsilon^n + s/k)^{1/n} - \epsilon \tag{1.2}$$

For particles of energy E less energy than E_r, on an average the entire energy E is deposited in the material. Thus, the deposited energy is exactly

$$E_{dep} = E, \qquad E \leq E_r \tag{1.3}$$

For energies E greater than E_r, there are two cases that must be differentiated: small and large energy deposition. If E_{dep} is small, it is appropriate to use (1.1) directly. Thus, we use for the average energy deposition

$$E_{dep} = s\,S(E), \qquad \begin{array}{c} s\,S(E)/E \leq .001 \\ E > E_r \end{array} \tag{1.4}$$

For larger energy deposition, we obtain by use of (1.1)

$$E_{dep} = (E + \epsilon) - \left[(E + \epsilon)^n - s/k\right]^{1/n}, \qquad \begin{array}{c} s\,S(E)/E > .001 \\ E > E_r \end{array} \tag{1.5}$$

Equation (1.5) goes over into (1.4) in the case $(E + \epsilon)^n \gg s/k$, which is equivalent to $s\,S(E)/E \ll 1$. The choice of .001 as the dividing point between use of (1.4) and (1.5) is arbitrary. Equation (1.5) is analytically correct for all $E > E_r$, of course. However, for small energy depositions, it requires the computation of the difference between the two large numbers in order to obtain a small one. In that instance, it is computationally more accurate to use (1.4) directly. For particles incident at an angle θ from the normal to an absorber of thickness x, the pathlength s is

$$s = x/\cos\theta \tag{1.6}$$

Thus, to find an energy deposition for a particle of energy E incident at angle θ on an absorber (detector or foil) of thickness x, first calculate E_r from (1.2). If

$E \leq E_r$, then use (1.3). Otherwise, calculate S(E) from (1.1). If $\epsilon S(E)/E \leq .001$, use (1.4); if not, use (1.5).

The constants ϵ, n, k depend upon the particle type, the absorber material, and the units used to describe the particle energy and absorber thickness. The following values have been used here:

TABLE 1.1

Energy Deposition Constants

Material →	Aluminum			Silicon		
Particle	ϵ (E in MeV)	n	k (s in mils)	ϵ (E in MeV)	n	k (s in μm)
Proton	0.257	1.781	0.3934	0.353	1.795	10.764
Alpha	1.222	1.794	0.03145	1.766	1.802	0.8665

For silicon, the theoretical stopping power data fitted were taken from Ref. 1.1; for aluminum, the proton data were taken from Ref. 1.2, while the alpha particle data came from Ref. 1.3. For protons, the range of validity is 0.5 - 100 MeV; for alphas, it is 2 - 200 MeV. The fit on S(E) is within about ±2% in all cases; over most of the range of validity it is much better. Characteristics of the detectors used in the engineering models and flight units are given in the following table:

TABLE 1.2

Telescope Detectors

	Eng. Model	Flight Units	Area
Front	46.9 μm	50 ± 1 μm	1.0 cm^2
Back	523.2 μm	512 ± 7 μm	2.0 cm^2

The thickness of these detectors was measured by an x-ray absorption method developed at Panametrics specifically for this purpose (Ref. 1.4). All three flight units are included within the thickness limits given.

By use of the above procedure and the thicknesses given, calculations have been made of the energy depositions (losses) in the front and back detectors by alpha particles and protons for both the engineering model and the flight units. Figure 1.2 shows results for the engineering model for 0° and 35° angles of incidence. On a graph such as this, the flight unit calculations are almost indistinguishable, hence they are not shown. The experimental measurements on the figure refer to data taken at the Brookhaven National Laboratory Tandem Van de Graaff accelerator facility. They provide verification of the analytical results.

Three energy bins are defined for each particle type: P1, P2, and P3 for protons and A1, A2, and A3 for alphas. As shown, the energy deposition thres-

Numbers attached to curves are incident particle energies (MeV)

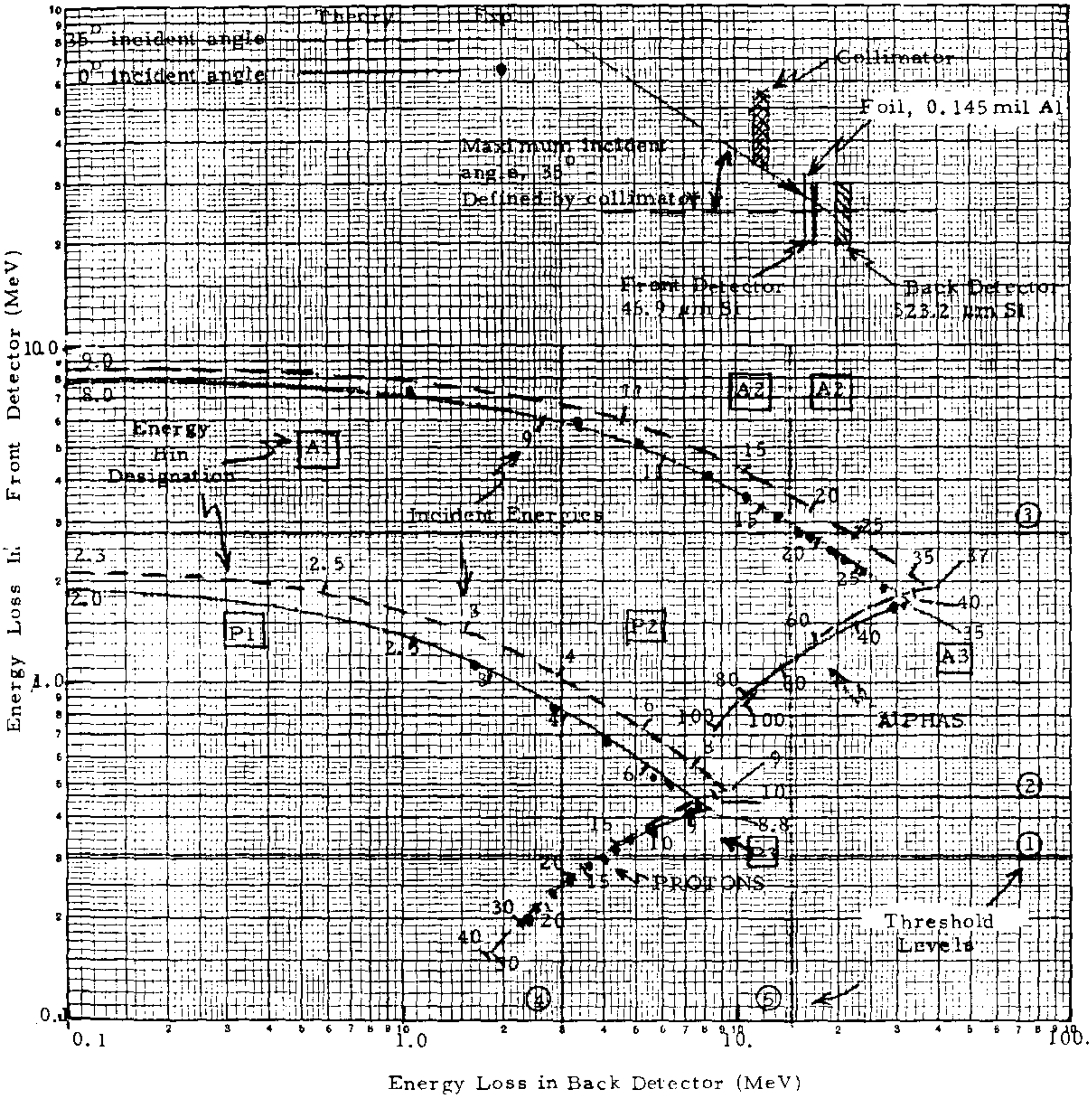

Figure 1.2 TELESCOPE ENERGY LOSS AND THRESHOLD LEVELS DIAGRAM - ENG. MODEL

holds 1 through 3 in the front detector, and 4 and 5 in the back detector, define the energy bins. However, the actual energy limits associated with any particular bin depend upon the angle of incidence of the particle. Thus, in order to define these in some average manner, we use an incidence angle of 20°. This is the location of the maximum in the geometrical factor (discussed below) variation with θ. Results are given in the following table.

TABLE 1.3

Telescope Energy Bin Limits and Logic for Engineering Model and Flight Units*

Threshold		Threshold Energy (MeV)		Coincidence-Anticoincidence Logic and Energy Bin Limits (MeV) Defined by Threshold					
#	Det. Loc.	Eng. Model	Flight Units	P1 $1\cdot 2\cdot \overline{3}\cdot \overline{4}$	P2 $1\cdot 2\cdot \overline{3}\cdot 4\cdot \overline{5}$	P3 $1\cdot \overline{2}\cdot 4\cdot \overline{5}$	A1 $1\cdot 3\cdot \overline{4}$	A2 $1\cdot 3\cdot 4$	A3 $1\cdot 2\cdot \overline{3}\cdot 5$
1	F	0.310	0.325	L = 0.6		U = 14.5			
2	F	0.460	0.490		U = 8.7	L = 8.7			
3	F	2.80	2.92				L = 3.8	U = 21.3	L = 21.3
4	B	3.00	3.20	U = 4.2	L = 4.2		U = 9.9	L = 9.9	
5	B	14.50	14.20						U = 61.0

*L, U = lower, upper limit of bin.
F, B indicates bin limit defined by threshold in front, back detector. All calculations for average energy loss and 20° angle of incidence.

It is seen that the bin limits are the same for the engineering model and all flight units. This is made possible, taking into account the difference in detector thicknesses of the engineering model and flight units, by using different energy deposition thresholds - as shown. Note that for all bins, except P1 and P3, threshold one coincidence is used only for timing purposes.

1.4 Experimental Observations Summary

1.4.1 Data Taking Periods

In order to obtain the necessary low energy data, it was decided that a request would be made to the Brookhaven National Laboratory Tandem Van de Graaff Program Advisory Committee (PAC). This was completed on April 10, 1978, with a request for 80 hours running time. The experiment was titled, "GOES Particle Sensor Calibrations", and was assigned experiment #188 by the PAC. The submission was supported by an April 28, 1978 letter to the PAC from Donald J. Williams, Director, Space Environment Laboratory, Environmental Research Laboratories, NOAA, Boulder, CO. In this letter, it was noted with regard to the GOES Energetic Particle Sensor that:

> "The Space Environment Laboratory of NOAA is the final user of this series of instruments. The data are used in real time by the Space Environment Services Center which is a part of our laboratory here in Boulder and is

archived for off-line use with World Data Center A. Although the data produced by the instrument directly is not of new exciting research potential, it is used to support many other geophysical experiments which are at the frontiers of physics. For instance, the GOES particle data are currently used in real time support of the International Ultraviolet Explorer satellite to help minimize radiation damage to the detectors. It will also form the basis for the control of radiation hazards to the operations of the NASA Space Shuttle."

Certainly, this information was of assistance in helping the PAC to make a decision on the application.

On 26 April a trip was made to BNL to view the set-up and to determine the interface equipment needed; and this was reported on to the PAC on 5 May 1978. Further submissions of information to the PAC were made on 9 June and 12 June 1978. Following the PAC meeting on 15 June 1978, we were notified on 19 June 1978 that a period of two days (~48 hours) running time had been approved.

Approximately 32 hours of the allotted time were used in the period 26 July - 1 August 1978. During this period some difficulty was experienced with a 5 mm thick Si(Li) monitor detector (discussed in detail in Ref. 1.5) used to determine the beam intensity. The most useful data were obtained for alpha particles in the second of the two 16-hour runs after a switch had been made to a 750 μm surface barrier detector as a monitor. All subsequent data were taken with this detector.

As a consequence of the monitor detector difficulty, a request for an additional 16-hour run (to bring requested total to 48 + 16 = 64 hours) was submitted on 14 August 1978. An additional 12 hours was approved (via telcon to B. Sellers) bringing the approved total to 48 + 12 = 60 hours. A 12-hour run was carried out on 12 September 1978, and a 16-hour run started at 2000 hours on 13 September 1978 and completed at 1200 hours on 14 September 1978. Thus, 60 hours of running time were carried out at BNL on protons and alphas (Refs. 1.5 and 1.6).

The high energy work was carried out at the Harvard Cyclotron, which provides a ~160 MeV proton beam. Data were taken during the 18 July - 20 July 1978 period with the Telescope Engineering Model and on 15 July 1979 with the Telescope Protoflight Model.

1.4.2 Energy/Angles Used

Calibration work on the SMS A, B, C and GOES B and C Telescope is detailed in References 1.7-1.9. As noted in Ref. 1.7, it was found as expected that for particles that penetrate the detectors the energy bins' limits depend upon the angle of incidence. However, in carrying out the detailed calibration work (Refs. 1.8 and 1.9), the only work done was for normal incidence ($\theta = 0$). To some extent, this was due to the difficulty of providing a method of varying θ under vacuum. Additionally, the maximum energy available on the Stanford Van de Graaff, where the work was done, was about 16 MeV for protons. For the present design, this would not have been sufficient to define the upper bin limits of the P3 bin (taking energy straggling effects into account). Thus, there were two principal objectives in the present calibration work on the new Telescope design:

1) determine effects of variation in angle of incidence
and
2) extend energy range upward to about 25 MeV for protons.

Both of these objectives were fulfilled by working at the BNL Van de Graaff. Additionally, the alpha energy range could be extended upward to about 40 MeV, although this was not sufficient to define the A 3 upper bin limit.

Figure 1.3 shows the general set-up of the monitor detector, EPS Telescope mounted on rotating platform, particle beam, scattering foil, and collimators. The scattering angle from the foil is $\beta = 24.5^\circ$. The angle of incidence θ of the scattered particles on the Telescope is controlled externally by rotating the platform by use of a rotating feed thru facility available at BNL. The monitor collimator aperture diameter is 0.25 in. and that of the beam collimators is .125 in.

The Telescope is shown held on its mount (a rectangular plate) in Figure 1.4. The rotating platform and gearing is shown. This rotating platform is also used at the Harvard Cyclotron; the set-up there is shown in Fig. 1.5, where there is no need to use a vacuum chamber because the 160 MeV proton beam exits directly into the laboratory. For that work, a series of disc-shaped plates can be mounted on the wheel shown (without plates). The wheel is then rotated (by remote control) to vary the energy incident on the Telescope. The right hand photograph in Figure 1.5 shows the Dome detector (not discussed here) held in the rotating platform mount. For this work, a remote controlled servo drive was used to vary θ. The monitor detector is behind a 2" thick brass collimator just to the left of the θ readout. The beam is rather broad, so the monitor and mounted instrument are exposed to very nearly the same intensity.

The set-up in the BNL vacuum chamber is given in Figure 1.6. As shown in Figure 1.3, the Telescope on the rotating platform is on the left and the monitor is on the right. Each views the scattering foil through holes in the copper plate. Because of symmetry, it is assumed that the intensity is the same at the two locations.

The Energy/angular values used at Harvard are summarized in Tables 1.4 and 1.5.

TABLE 1.4

EPS Engineering Model Telescope
Proton Data Taken at Harvard Cyclotron
(Energies In MeV)

Data Period:
18 July - 20 July 1978*

*Data in Notebook GOES EPS #2: p.28 and 33 for E_{in} = 144 and 124 MeV, all other data on p.33.

E_{in}	Angles of Incidence (deg)
144	0, 15, 30, 45, 60
133	0
128	0, 10
124	0
108	0
79	0
45	0
33	0

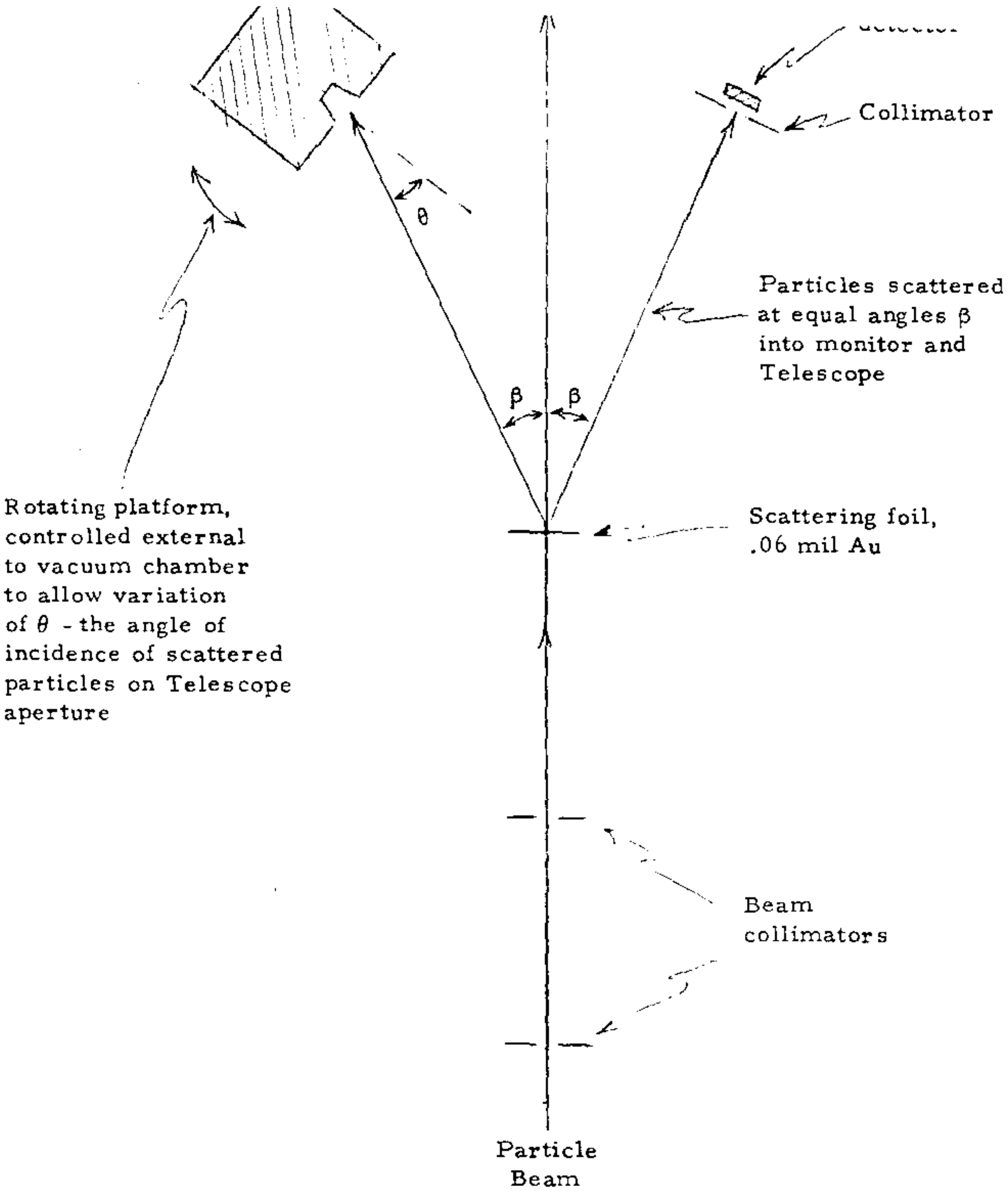

Figure 1. 3 General Experimental Set-up at Brookhaven National Laboratory.

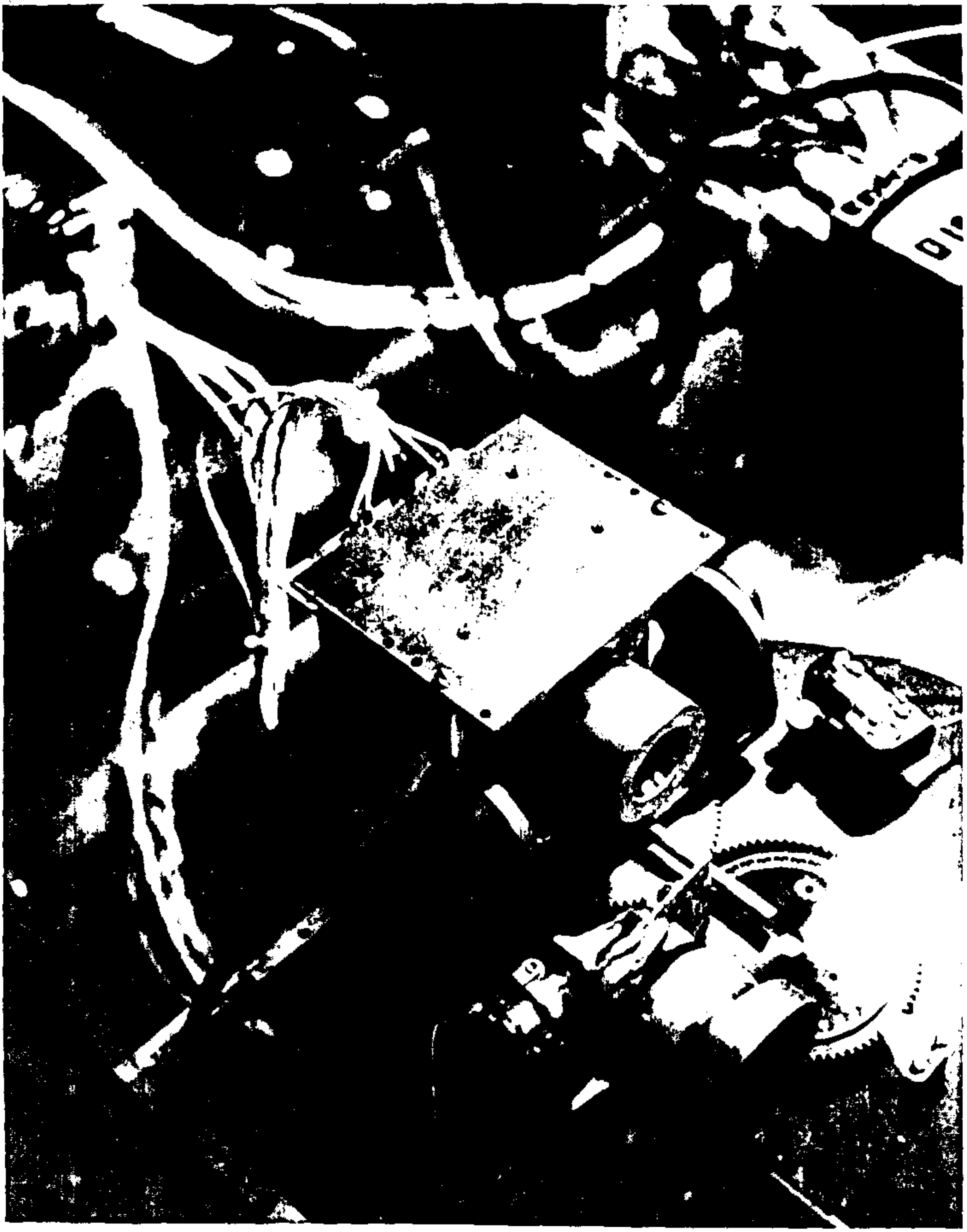

Figure 1.4 Telescope on Rotating Platform Mount

Fig. 1.5 SET-UP AT HARVARD CYCLOTRON

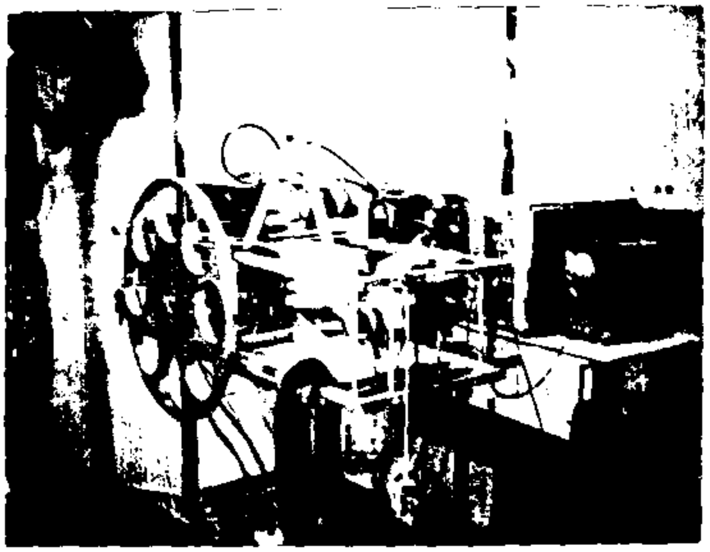

General set-up showing wheel for mounting absorbers to vary incident energy.

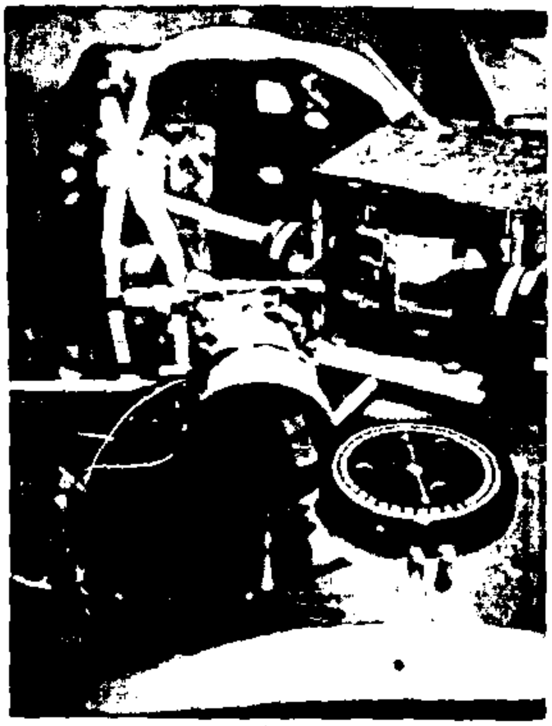

↑ Beam Direction

Fixed monitor detector and Dome mounted on rotating assembly.

Fig. 1.6 SET-UP AT BNL

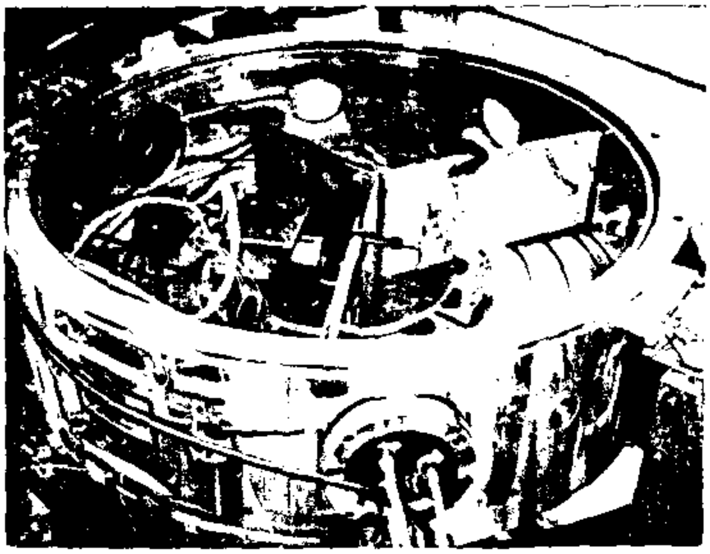

View of scattering chamber showing Telescope mounted on rotating assembly.

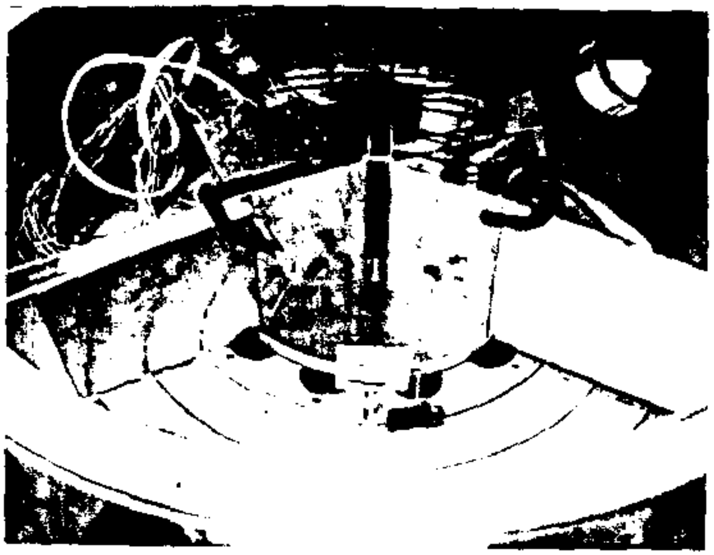

↑ Beam Direction

View from beam direction. Monitor and Telescope view scattering foil thru holes in thick copper plate - monitor is behind hole on right.

TABLE 1.5

EPS Protoflight Model Telescope
Proton Data Taken at Harvard Cyclotron
(Energies in MeV)
Data Period: 15 July 1979*

E_{in}	Angles of Incidence (deg)
90	180, 165, 150, 135, 120
79	180, 165, 150, 135
70	180, 165, 150
60	180

*Data Summary in Notebook GOES EPS#4, p. 59-60

It will be noted that some work was done with the Protoflight model, as given in Table 1.5.

Work done at BNL is summarized in Tables 1.6 and 1.7 for protons and alpha particles.

TABLE 1.6

EPS Engineering Model Telescope
Proton Data Taken at BNL
(Energies in MeV)
Data Period: 12 September - 14 September 1978*

E_b	E_{in}	E_b	E_{in}
25	25.0	9.0	8.9
23	23.0	8.0	7.9
22	22.0	7.0	6.9
21	21.0	6.0	5.9
20	20.0	5.5	5.4
18	18.0	5.0	4.9
17	17.0	4.5	4.4
16	16.0	4.0	3.9
15	15.0	3.5	3.4
14	14.0	3.0	2.9
13	13.0	2.5	2.4
12	12.0	2.0	1.9
11	11.0	1.5	1.3
10	10.0		

*Angles covered were 0° to +40° at 5° intervals at all energies. For 6 MeV protons, the angles covered also included 0° to -35° at 5° intervals.

Energies shown are beam energy E_b and energy E_{in} incident on detectors after passing through .06 mil Au scattering foil.

Data recorded in Notebook GOES EPS#4 p. 5-10, 19-20, 26-31, and 37-39

TABLE 1.7

EPS Engineering Model Telescope
Alpha Particle Data Taken at BNL
(Energies in MeV)

Data Period:*
30 July - 1 August 1978

E_b	E_{in}
10.0	9.5
9.0	8.5
8.0	7.4
7.0	6.4
6.2	5.5
5.5	4.8
4.5	3.7

Data Period:**
12 September - 14 September 1978

E_b	E_{in}
36	35.8
34	33.8
30	29.7
26	25.7
24	23.7
23	22.7
22	21.7
21	20.7
20	19.7
19	18.7
17	16.6
15	14.7
13	12.6
11	10.5
10	9.5
9	8.5
8	7.4
6	5.3
5	4.2

*Angles covered were -5° to +35° at 5° intervals at all energies except at E_b = 5.5 MeV; angles were -40° to +35° at 5.5 MeV.

Data in Notebook GOES EPS #2; p. 59-70, 76-82

**Angles covered were 0° to +40° at 5° intervals at all energies.

Data in Notebook GOES EPS #4, p. 14-18, 32-36

2. PRIMARY GEOMETRICAL FACTOR DETERMINATION

2.1 Method of Approach

2.1.1 Basic Energy Dependent Geometrical Factor

For a detector such as the telescope in Figure 1.1, the count rate per unit solid angle $C(E, \Omega)$, cps/sr, due to an angular flux of particles of energy E from direction Ω, $F(E,\Omega)$, p/(cm^2 - sr -sec), can be written

$$C(E,\Omega) = dC_o(E,\Omega)/d\Omega = F(E,\Omega)\, A(E,\Omega) \qquad (2.1)$$

where $A(E,\Omega)$, cm^2, is the effective area of the sensor in the direction of Ω, and C_o, cps, is the count rate found by integrating over Ω:

$$C_o(E) = \int F(E,\Omega)\; A(E,\Omega)\; d\Omega \qquad (2.2)$$

For an isotropic angular flux, F can be removed from the integral, and

$$C_o(E) = F(E) \int A(E,\Omega)\; d\Omega \qquad (2.3)$$

$$= F(E)\;\; G(E) \qquad (2.4)$$

where $G(E) = \int A(E,\Omega)\; d\Omega \qquad \text{cm}^2 - \text{sr} \qquad (2.5)$

is the isotropic geometrical factor for energy E. For an analytical determination of G(E), it is convenient to express the count rate per unit solid angle $C(E,\Omega)$ as a function of $F(E,\Omega)$ and the detection system parameters, and then find $A(E,\Omega)$ by use of (2.1):

$$A(E,\Omega) = C(E,\Omega)/F(E,\Omega) \qquad (2.6)$$

This result is then placed in (2.5) and integrated over Ω to find G(E).

Experimentally, the particle beam in Figure 1.3 is almost monodirectional, so that the solid angle is quite small. In that case, it is convenient to write $A(E,\Omega)$ from (2.1) as

$$A(E,\Omega) = \frac{dC_o\,(E,\Omega)}{F(E,\Omega)\, d\Omega} \approx \frac{\Delta C_o\,(E,\, \Omega)}{\Delta I\,(E,\Omega)} \qquad (2.7)$$

where, in direction Ω, ΔC_o is the increment of count rate produced by a measured increment of essentially monodirectional angular intensity

$$\Delta I(E,\Omega) = F(E,\Omega)\,\Delta\Omega \qquad \text{p/(cm}^2 - \text{sec)} \qquad (2.8)$$

Thus, in both the analytical and experimental cases, the isotropic geometrical factor is found by use of Eq. (2.5).

For determination of $A(E, \Omega)$, however, (2.7) is better for the experimental determination of $G(E)$, while (2.6) is used for the analytical approach. Furthermore, we note that there are variables upon which the count rate depends that are not shown in (2.6) or (2.7). These are assumed to be contained implicitly and are discussed below.

2.1.2 Experimental Energy Dependent Geometrical Factor

Experimentally, as described in Section 1, the approach is to irradiate the telescope at different angles of incidence with a particle flux of known intensity, having known energy, and measure the counts produced. In that way, the geometrical factor is defined by use of (2.7) and (2.5). The intensity ΔI is just the rate at which particles are incident on a spherical surface, in part/(cm^2 - sec), which is obtained by measurement of the counts C_m recorded in some time t by the monitor detector, (Figure 1.2) whose area is A_m. Then, the intensity is $C_m/(A_m t)$, (cm^2 - sec)$^{-1}$ at the monitor detector. But the telescope is located at exactly the same distance from the scattering foil, and at the same scattering angle β. Thus, the intensity there is assumed to be the same, and

$$\Delta I = C_m/(A_m t) \tag{2.9}$$

During this time t the counts recorded in the telescope are C_t. Hence, by replacing the integral with a summation over the number of values of i used, we obtain

$$G(E) = \frac{A_m t}{t} \sum_i \frac{C_t(\theta_i)}{C_m(\theta_i)} \Delta\Omega_i \tag{2.10}$$

Thus, $C_t(\theta_i)$ and $C_m(\theta_i)$ are the values of those quantities recorded while the telescope is oriented at θ_i degrees to the incident particle direction. These can vary with time, of course, but use of the monitor in this way eliminates the temporal effects. Hence, t cancels in (2.10) and the result is

$$G(E) = \sum_i N(\theta_i) G_i \tag{2.11}$$

where the number of telescope counts observed per monitor count, while the telescope is oriented at angle θ_i, is

$$N(\theta_i) = C_t(\theta_i)/C_m(\theta_i) \tag{2.12}$$

and a geometrical factor associated with the particular measurement at angle θ_i is

$$G_i = A_m \Delta\Omega_i \tag{2.13}$$

which, because of symmetry in the azimuthal angle, is

$$G_i = 2\pi A_m \sin\theta_i \, \Delta\theta_i \tag{2.14}$$

Here $\Delta\theta_i$, radians, is the width of the θ bin centered on θ_i.

The procedure then is to measure $C_m(\theta_i)$ and $C_t(\theta_i)$ at a series of values of θ_i. $N(\theta_i)$ is calculated from (2.12), and since A_m is known, the G_i are found from (2.14). Then G(E) is calculated from (2.11).

2.1.3 Analytical Energy Dependent Geometrical Factor

2.1.3.1 General Equation

Figure 2.1 is a scaled enlargement of the portions of Figure 1.1 needed for this calculation. From Figure 1.1, it is apparent that any particle passing through the "Detection Aperture" of Figure 2.1 will be counted if it produces a pulse of proper size for one of the energy bins.

For the analytical determination of G(E), use is made of Eqs. (2.6) and (2.5). Here, we write explicitly the variables upon which C, cps/sr, depends. Thus,

$$C(E, E_1, E_2, \Delta E_n, \Delta E_s, \theta) = F(E,\Omega) \cos\theta \, A_{eff}(\theta) \, P(E, E_1, E_2, \Delta E_n, \Delta E_s, \theta) \quad (2.15)$$

Hence, in Eq. (2.1) the effective <u>sensor</u> area $A(E,\Omega) = A_{eff} P \cos\theta$. Now, since $F(E,\Omega)$ is the angular flux, $F \cos\theta$ is the flux in the plane of the detection aperture. All particles passing through the entrance aperture do not, however, pass through the detection aperture; the fraction that do depends upon the angle of incidence θ. For $\theta \leq 35^\circ$, the effective <u>detection</u> area, A_{eff}, is just the overlap area formed by projection of the entrance aperture on the detection aperture, as shown in the top left in the figure. Rays incident at angles $\geq 37^\circ$ are totally obscured by the Collimator. Between 35° and 37°, the rays are partially obscured by the collimator, hence, the effective area is less than the Overlap area. $A_{eff}(\theta)$ is discussed in Section 2.1.3.2 below.

In general, the quantity P in (2.15) must be the probability that a particle of energy E incident at angle θ will produce a count. Table 1.3 (p. 6) shows that, strictly speaking, an analytical calculation will require determination of the energy losses in both detectors for <u>all</u> bins except P3. However, in order to investigate the possibility of making an analytic calculation of the geometrical factor, we provide below the expression for the particular case in which the response is defined by only one detector, and the particle has sufficient energy to penetrate the detector. For P3, this is the front detector.

As discussed in Section 1, and shown by the calculations in Figure 1.2, it is straightforward to calculate the <u>average</u> energy loss in such a detector. However, there is a distribution of <u>energy losses</u> about this <u>average</u>, which is almost Gaussian (Ref. 2.1) for the energy losses here. The situation is further complicated by the fact that a <u>pulse</u> distribution (also nearly Gaussian) will be produced by a series of energy losses all of the <u>same</u> magnitude. This is caused by electronic noise. Thus, a particle of energy E incident on a detector produces a distribution of pulses that is a convolution of energy loss (straggling) and noise distributions, characterized by FWHMs of ΔE_s and ΔE_n, respectively. The probability P thus depends on E, θ, ΔE_s, ΔE_n, and the lower and upper pulse height (energy) thresholds E_1 and E_2 of the bin. In practice, the expression can also be applied to find the variation of C(E) in the vicinity of <u>any</u> one threshold, provided the effect of the other

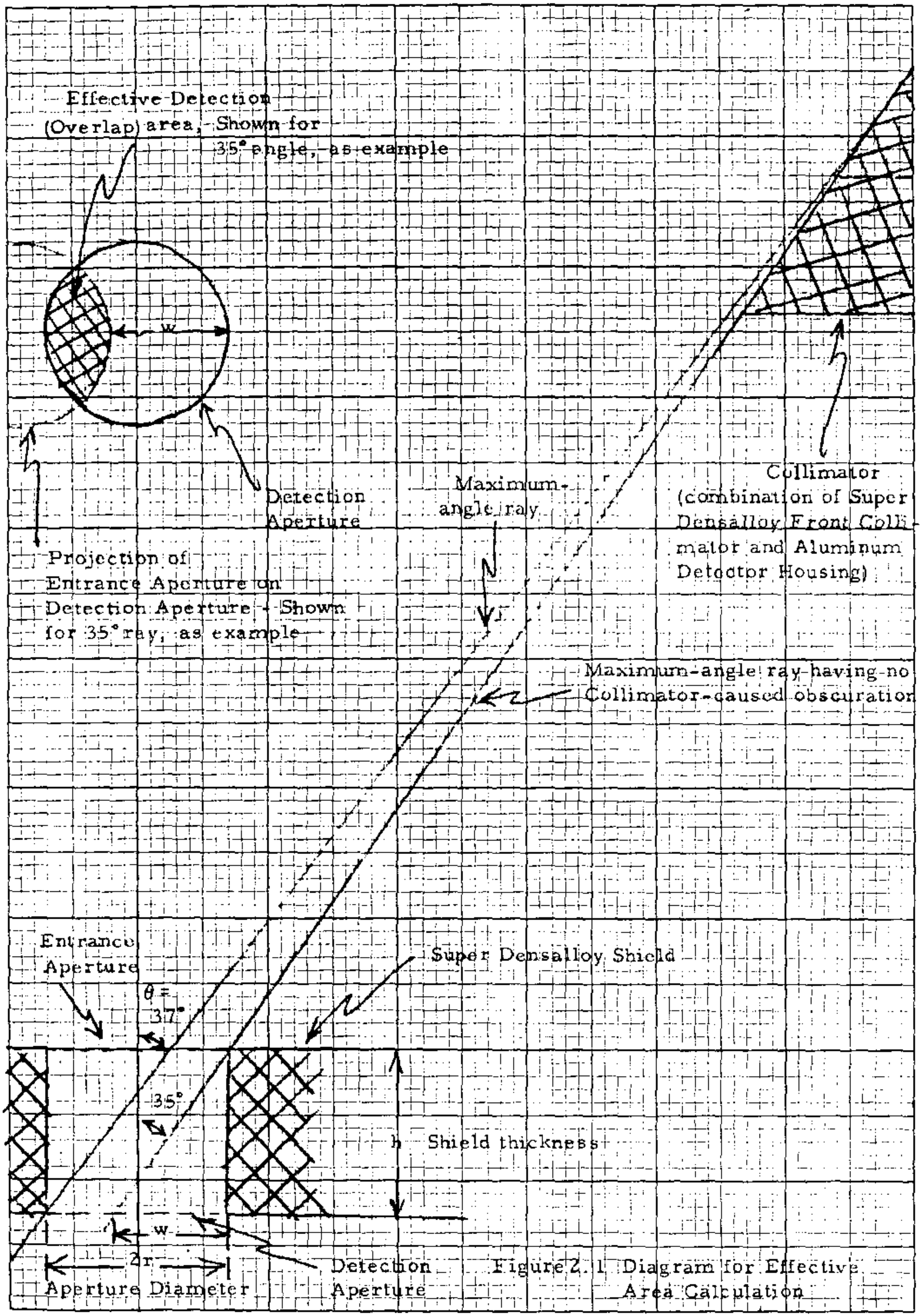

Figure 2.1 Diagram for Effective Area Calculation

threshold is small in that energy range. For example, as can be judged from Figure 1.2 (p. 5), for bin P2 the effect of threshold 4 (in the back detector) is very small for protons that deposit energies in the front detector near the threshold 2. Those protons deposit an average of about 7 - 9 MeV in the back detector, which is more than twice the energy of threshold 4. Since the width of the energy loss straggling distributions is on the order of 0.1 MeV, there is, therefore, little chance that such a proton will produce a pulse that does not exceed threshold 4. The expression for P is given in Section 2.1.3.3 below.

2.1.3.2 Effective Area

Neglecting collimator-induced obscuration, the effective area $A_{eff}(\theta)$ is the overlap area formed by projection of the entrance aperture on the detection aperture. It is shown as the area of intersection of two circles of radius r in Figure 2.1 and reproduced below:

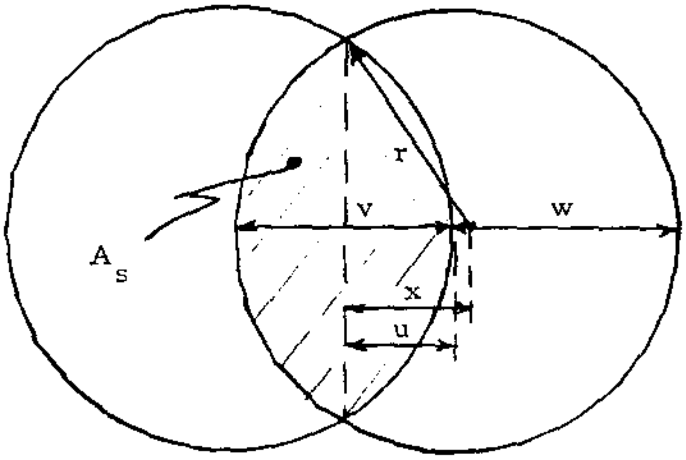

Figure 2.2 Diagram for Intersection Area Calculation

From the standard formula for the area of a sector of a circle, we have the intersection area A_s

$$A_s = 2\left\{\frac{\pi r^2}{2} - \left[x\sqrt{r^2 - x^2} + r^2 \sin^{-1}\left(\frac{x}{r}\right)\right]\right\}$$

$$= \pi r^2\left[1 - \frac{2u}{\pi}\sqrt{1 - u^2} - \frac{2}{\pi} \sin^{-1} u\right] \tag{2.16}$$

where $u = x/r$

In order to use this expression, we must express x in terms of h and θ. Thus, from the above figure, it is seen that

$$v = r - (w - r) = 2r - w$$

$$u = v/2 = r - w/2$$

so $$x = u + w - r = r - \frac{w}{2} + w - r = w/2$$

but $$w = h \tan\theta \quad \text{(from Figure 2.1)}$$

so $$x = \frac{h}{2} \tan\theta$$

which is the desired expression, and thus

$$u = \frac{h}{2r} \tan\theta \tag{2.17}$$

for use in (2.16).

For $\theta \leq 35°$, $A_{eff} = A_s$. For $37° > \theta > 35°$, the collimator partially obscures the intersection area, and for $\theta \geq 37°$ the obscuration is complete. Thus, we define the following correction function

$$\left.\begin{array}{lll} C_s(\theta) = 1 & & \theta \leq 35° \\ C_s(\theta) = (37 - \theta)/2 & & 35° < \theta < 37° \\ C_s(\theta) = 0 & & 37° \leq \theta \end{array}\right\} \tag{2.18}$$

which produces a linear obscuration over the 2° affected by the collimator. Then,

$$A_{eff}(\theta) = A_s(\theta)\, C_s(\theta) \tag{2.19}$$

with A_s given by (2.16), u by (2.17) and $C_s(\theta)$ by (2.18). For the Telescope,

$$\left.\begin{array}{l} h = 0.125'' \\ r = 0.070'' \end{array}\right\} \tag{2.20}$$

2.1.3.3 Detection Probability

2.1.3.3.1 Gaussian Approximation

As discussed with regard to Eq. (2.15), the quantity P is just the probability that a particle of energy E, incident at angle θ on a detector characterized by an electronic noise induced distribution having FWHM of ΔE_n, will produce a pulse with height between thresholds E_1 and E_2. Interaction of the particle with the detector produces a "straggling" distribution of energy losses having a FWHM of ΔE_s. Here, for simplicity, we restrict the analytical development to the case of an energy bin defined by thresholds E_1 and E_2 in a single detector (such as bin P3), or to the case in which the response near one threshold is nearly independent of the value of the other threshold (as for threshold 2, bin P 2, which is nearly independent of the effects of threshold 4).

Here we will assume that both the noise and straggling distributions are essentially Gaussian. The convolution of two such distributions produces another Gaussian which can be characterized by an exponential width E_w, so that the probability P can be written

$$P = \int_{E_1}^{E_2} P_o \, e^{-(E_p - E_d)^2 / E_w^2} \, dE_p \tag{2.21}$$

Here E_p is the energy loss pulse height produced by interaction of the particle of energy E with the detector, and E_d is its average value, E_{dep} discussed in Section 1.3. There are several equivalent ways to express the width of a Gaussian distribution. These are related as follows:

$$E_w^2 = 2\sigma^2 = k^2 \Delta E^2 \tag{2.22}$$

where σ is the "standard deviation", and ΔE is the full width at half maximum, "FWHM". The value of k is

$$k = \frac{1}{2\sqrt{\ell n\, 2}} \approx .601 \tag{2.23}$$

The fact that the convolution of two Gaussians produces a Gaussian means that

$$\Delta E^2 = \Delta E_n^2 + \Delta E_s^2 \tag{2.24}$$

which is a convenient representation from the viewpoint of the noise effect, because it is ΔE_n that is usually specified. However, the energy straggling effect is normally discussed in terms of σ_s, the straggling standard deviation. From (2.22), we obtain

$$\begin{aligned} \Delta E_s^2 &= 2\sigma_s^2 / k^2 = (8\, \ell n\, 2)\, \sigma_s^2 \\ &\approx 5.545\, \sigma_s^2 \end{aligned} \tag{2.25}$$

Thus, given σ_s^2 and ΔE_n^2, ΔE_s^2 is found from (2.25), ΔE^2 from (2.24), and E_w^2 from (2.22). σ_s is discussed in the following section.

Now, P must be normalized to unity so that it represents a probability.

Hence, we require

$$1 = P_o \int_0^E e^{-(E_p - E_d)^2/E_w^2} \, dE_p \tag{2.26}$$

The minimum possible pulse height E_1 is clearly 0, and the maximum E_2 is the particle energy E. From (2.26), the normalization constant P_o is^2 found to be

$$P_o = \left\{ \frac{E_w\sqrt{\pi}}{2} \left[\operatorname{erf}\left(\frac{E - E_d}{E_w}\right) + \operatorname{erf}\left(\frac{E_d}{E_w}\right)\right]\right\}^{-1} \tag{2.27}$$

where the error function is defined by

$$\operatorname{erf}(x) = \frac{2}{\sqrt{\pi}} \int_0^x e^{-u^2} \, du \tag{2.28}$$

Integration of (2.21) and use of (2.27) causes the term $E_w\sqrt{\pi}/2$ to cancel. Noting that erf(-x) = -erf(x) yields

$$P = \frac{\operatorname{erf}(T_2) - \operatorname{erf}(T_1)}{\operatorname{erf}(T_{20}) + \operatorname{erf}(T_{10})} \tag{2.29}$$

where

$$\left.\begin{aligned} T_2 &= (E_2 - E_d)/E_w \\ T_1 &= (E_1 - E_d)/E_w \\ T_{20} &= (E - E_d)/E_w \\ T_{10} &= E_d/E_w \end{aligned}\right\} \tag{2.30}$$

In order to evaluate erf(x), we have made use of a rational approximation (Ref. 2.2, Eq. 7.1.2.6).

This completes the determination of the count probability P, except for expressing ΔE_s in terms of E and the detector characteristics. This is discussed below.

2.1.3.3.2 Energy Loss Straggling

When a particle passes through a detector whose thickness is small compared to the particle's range, the average energy deposited in the detector- and lost by the particle- can be calculated as in Section 1.3. There is, however, a distribution of energy losses around this average that can be characterized by some standard deviation σ_s. In the most general case, this distribution can be highly asymmetrical, with a most probable energy loss that differs significantly from the average energy loss. This occurs, for example, when relativistic protons lose extremely small amounts of energy in a detector. The general distribution of Vavilov has been treated by Seltzer and Berger (Ref. 2.1), and under some rather wide ranges of energy loss, the general distribution can be approximated quite well by a Gaussian (Ref. 2.1, Eq. 15). Certain corrections to this distribution have been made by Bichsel (Ref. 2.3, Eq. 4). From Refs. 2.1 and 2.3, we can write

$$\sigma_s^2 = \xi^2(1 - \beta^2/2)\, F_c/K \tag{2.31}$$

Here, β is the ratio of the particle's velocity to that of light, determined as follows:

$$\left.\begin{aligned} \beta^2 &= T(T+2)/(T+1)^2 \\ &\approx 2T \qquad T \ll 1 \end{aligned}\right\} \tag{2.32}$$

$$\text{where } T = E/(Mc^2) \tag{2.33}$$

E is the particle's kinetic energy, and Mc^2 is its rest mass energy. For protons

$$Mc^2 = 938 \text{ MeV} \tag{2.34}$$

The quantity ξ is defined as follows:

$$\xi = vs/\beta^2 \tag{2.35}$$

where s, g/cm^2, is the detector thickness in the direction of travel of the particle-the pathlength-and

$$v = .30058\, mc^2\, (Z/A)z^2 \tag{2.36}$$

$$mc^2 = .511 \text{ MeV} = \text{electron rest mass energy} \tag{2.37}$$

$$z = \text{no. electronic charges on particle} \tag{2.38}$$

$z = 1$ for protons and $z = 2$ for alpha particles. Z is the atomic number and A the atomic weight for the detector material. For silicon, the detector material of interest here,

$$Z/A = .4984 \tag{2.39}$$

The quantity K is defined by

$$K = \xi / \epsilon_{max} \tag{2.40}$$

where ϵ_{max} is the maximum energy transfer in a single collision, given approximately by

$$\epsilon_{max} = \frac{2\, mc^2 \beta^2}{1 - \beta^2} \tag{2.41}$$

which is correct for $\beta^2 \ll 1$ and $m \ll M$, both good approximations here.

F_c is the correction factor derived from results of Bichsel (Ref. 2.3)

$$F_c = Q' (1 + q) \tag{2.42}$$

q is a quantum mechnical correction, defined in terms of β^2:

$$\left.\begin{aligned} q &= (0.00186/\beta^2)\, \ln (102\, \beta^2 + 0.746) \\ &\qquad\qquad 0.0005 < \beta^2 < 0.0075 \\ &= (0.0009/\beta^2)\, \ln (306\, \beta^2) \\ &\qquad\qquad 0.0075 < \beta^2 \end{aligned}\right\} \tag{2.43}$$

Q' is a factor that takes into account the increase in straggling due to spread in energy as the particle passes through the detector. It is defined by Bichsel (Ref 2.3, Eq. 8) at three values of the stopping number B, which can be expressed as (see Ref. 2.3, Fig. 4)

$$B = \frac{S\, \beta^2}{.1531\, z^2} \tag{2.44}$$

Here, S is the stopping power, Eq. (1.1). We have fitted the three values of Q' given by Bichsel to a power law form and obtained the following result:

$$Q' = .99 \left(\frac{E}{E - E_d} \right)^u, \quad 2.3 < B < 6.9 \tag{2.45}$$

with

$$u = .59 (\ln .5577 B)^{.4114} \tag{2.46}$$

This allows calculation at all values of E for which B lies in the range given in (2.45). Thus, to find F_c for a given E, S is found from (1.1), β^2 from (2.32), q from (2.43), B from (2.44), u from (2.46), E_d from Section 1.1, Q' from (2.45), and F_c from (2.42). Since q is positive and Q' is generally somewhat larger than unity, the correction factor F_c is a number greater than unity. Hence, its effect is to increase the width of the straggling distribution.

Now using the above results and specializing to the case of silicon, we obtain by use of (2.31) in (2.25),

$$\Delta E_s^{\ 2} = 0.4338\, z^2 \left(\frac{1 - \beta^2/2}{1 - \beta^2} \right) F_c\, s \qquad \mathrm{MeV}^2 \qquad (2.47)$$

The pathlength s through the detector in the direction θ of the particle's travel is given in terms of the detector thickness x, g/cm^2, by Eq. (1.6). Eq. (2.47) is the result that is used in (2.24) along with ΔE_p to find ΔE. E_w is then calculated from (2.22), and the probability P is found from (2.29).

2.1.3.4 Geometrical Factor Equation

Now substituting P from (2.29), and $A_{eff}(\theta)$ from (2.19) into (2.15), placing the result in (2.6), and making use of (2.5), yields

$$G(E) = \int_\Omega A_s(\theta)\, C_s(\theta) \left\{ \frac{\mathrm{erf}(T_2) - \mathrm{erf}(T_1)}{\mathrm{erf}(T_{20}) + \mathrm{erf}(T_{10})} \right\} \cos\theta \, d\Omega \qquad (2.48)$$

As expected, the angular flux dependence cancels, and G(E) depends only on the detection system parameters. Here, A_s and C_s are found from (2.16) and (2.18), and the T's are defined in (2.30). For use in (2.30), the energy deposition E_d for particle energy E is calculated as in Section 1.3, and E_w is found from (2.22) by the procedure discussed in Section 2.1.3.3.2.

The integral is carried out over the aperture. Because the telescope possesses azimuthal symmetry, that integral yields 2π, and the Ω integral reduces to an integral over θ, with

$$d\Omega = 2\pi \sin\theta \, d\theta \qquad (2.49)$$

The integral must be determined numerically due to the complexity of the analytical functions in the integrand. This is discussed in Section 2.2 below.

2.1.4 Average Geometrical Factor

At times it is adequate not to take into account the detailed energy dependency of the flux within a given energy region, such as in each channel, but to make the approximation that, essentially, the flux is constant within the region.

Here, we will present results for an isotropic differential (in energy) angular flux spectrum f(E), (cm^2 - sec - sr - MeV)$^{-1}$. The number of particles between E and E + dE is then f(E) dE, and the count rate for a specified G(E) is

$$c = \int f(E)\ G(E)\, dE \tag{2.50}$$

If it is assumed that f(E) is essentially constant over the region of interest, defined by "limits" E_{1i} and E_{2i}, then

$$f(E) \approx \overline{f}(\overline{E})$$

where $\overline{E} = (E_{2i} + E_{1i})/2$ (2.51)

is the average energy characterizing that region, and

$$c(E) \approx \overline{f}(\overline{E}) \int G(E)\, dE$$

Now the integral can be written

$$\overline{G}(E)\, \Delta E \equiv \int G(E)\, dE$$

where $\Delta E = E_{2i} - E_{1i}$ (2.52)

thus defining $\overline{G}(E)$ as

$$\overline{G}(E) = \frac{1}{\Delta E} \int G(E)\, dE \tag{2.53}$$

Hence, c(E) can be expressed as

$$c(E) = \overline{f}(E)\, \overline{G}(E)\, \Delta E \tag{2.54}$$

within the approximate range ΔE.

Given the count rate and $\overline{G}(E)\ \Delta E$, the average flux in the region is given by:

$$\overline{f}(E) = c(E)/(\overline{G}(E)\ \Delta E) \tag{2.55}$$

In the case of the primary geometrical factor determination, there is generally only one value of $\overline{G}(E)$ of interest: that averaged over the channel limits and called the "channel average geometrical factor". However, for spurious responses, there may be several energy regions which contribute to a given energy channel; and those are called the "spurious average geometrical factors" for a given energy channel. Effectively, the calculated spurious counts in the channel of interest must be subtracted from observed counts before the average flux in the channel can be defined by use of (2.55).

The quantity $\overline{f}(E)$ determined from (2.55) is then to be interpreted as the approximate number of particles/(cm^2 - sec - sr - MeV) in the region E_{1i} to E_{2i}. It is a relatively crude approximation, which can be improved significantly by straightforward reiteration methods involving assumptions about the dependence of f(E) on E, other than that f(E) is constant within the region. The details of such approaches are beyond the scope of the present effort, however, (See Ref. 2.4 for some examples).

2.2 Results

2.2.1 Energy Dependent Geometrical Factor

2.2.1.1 Experimental

The experimental data are in the form of the number of counts, C_t, recorded in a given energy channel at angle θ during the time t required for the monitor detector to record a fixed number of counts, usually 10^4 for reasons of statistical accuracy. This allows a determination of $N(\theta)$, as defined in Eq. (2.12), which is the quantity of interest. From the values of $N(\theta)$ at the various values of θ, the energy dependent geometrical factor, G(E), is determined by use of Eq. (2.11).

The particle energies and angles used at BNL Tandem Van de Graaff for the Engineering Model Telescope are given in Tables 1.6 and 1.7. Table 2.1 below summarizes the angles, θ_i, and associated geometrical factors, G_i, found from Eq. (2.14). As noted previously, the diameter of the monitor detector aperture was 0.25", which corresponds to an area

$$A_m = 0.3167 \text{ cm}^2 \tag{2.56}$$

TABLE 2.1

Angular Bins and Associated Geometrical Factors used at BNL*
with Engineering Model Telescope

Bin #	θ_i (°)	$\Delta\theta_i$ (°)	$\Delta\Omega_i$ (sr)	G_i (cm^2-sr)
1	1.25	2.5	5.98 - 3	1.89 - 3
2	5.0	5.0	4.78 - 2	1.51 - 2
3	10.0	5.0	9.52 - 2	3.02 - 2
4	15.0	5.0	1.42 - 1	4.49 - 2
5	20.0	5.0	1.88 - 1	5.94 - 2
6	25.0	5.0	2.32 - 1	7.34 - 2
7	30.0	5.0	2.74 - 1	8.68 - 2
8	35.0	5.0	3.14 - 1	9.96 - 2

*Read N - n as N x 10^{-n}

Bin #1 data were actually taken at $\theta = 0^\circ$, but are assigned to $\theta = 1.25^\circ$ to provide continuity in the boundaries of the angular bins. Thus, the data in each bin belong to the angular range $\theta_i \pm \Delta\theta_i/2$.

The variation of $N(\theta_i)$ with E for each of the values of θ_i in the table is plotted in Figures 2.3 - 2.10 for the proton channels and in 2.11 - 2.18 for the alpha particle channels. The continuous curves have been drawn by eye as fits to the data. Although 40° incidence angle data are not given here, they were recorded, and the counts do go to zero at that angle in all channels.

For use in Eq. (2.11), the values of $N(\theta_i)$ were read from the continuous curves in the data plots. The values of G_i were taken from Table 2.1, with results given in Figures 2.19 and 2.20. Also shown in Figure 2.19 are the results of the analytical approach for channel P3 and a portion of channel P2. These results are discussed in the next section.

When compared with Table 1.3, it is observed from the figures that the channel limits are correct experimentally within a few tenths MeV for both particles and angles. This verifies the calculations for both detectors, the detector thickness measurements, and the coincidence and counting circuitry.

Two factors require explanation in the proton data. At high energies (channel P3), some particles are not counted due to loss below discriminator level 1 as a result, principally, of energy loss straggling in the front detector. Thus, the P3 decrease at high energies is not sharp. In fact, the maximum value of G(E) near 12 MeV does not quite reach the theoretical maximum of about $.055\ \mathrm{cm}^2$ - sr because of this effect.

In the low energy proton bin, P1, the geometrical factor exceeds that expected (the alpha particle low energy geometrical factor is generally as expected). The scattering cross section from the foil is proportional to the factor:

$$\sin^{-4}(\beta/2)$$

which varies strongly with β. A 20% variation in scattered intensity is caused by about 1° variation in β. Such a variation could easily be caused by the earth's field (for 1-5 MeV protons) following the last focussing magnets in the beam line. The effect would be much less for alphas due to their greater mass. A similar effect, although not as large, was also seen in the GOES B and C instruments (see Aeronutronic Report Ref. 1.8, p. 22). We believe these low energy proton data should probably be normalized downward somewhat, in such a way that the peak of G(E) is as expected, while the variation of G(E) with E is retained.

2.2.1.2 Analytical

Equation (2.48) is the expression used for analytical determination of

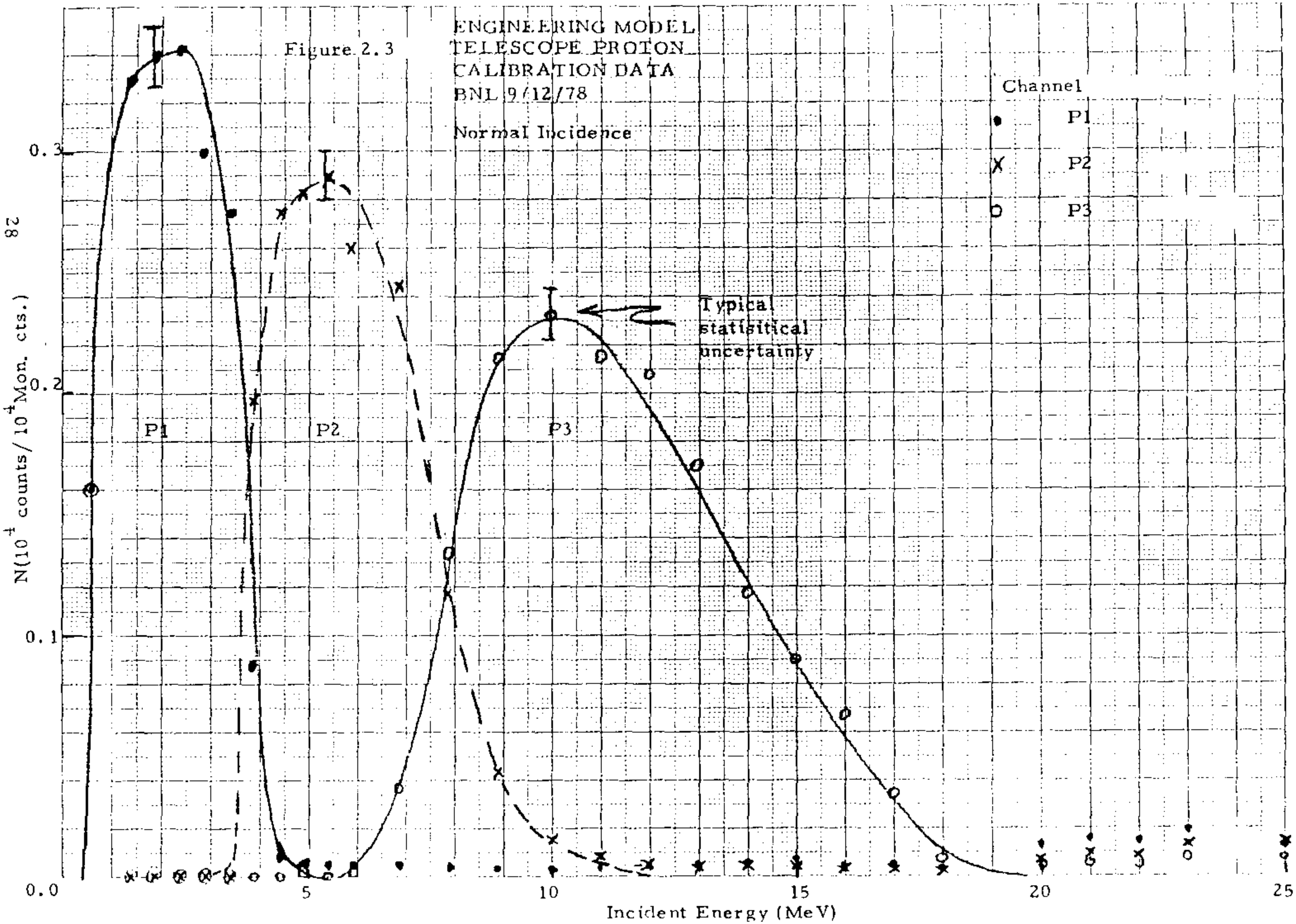

Figure 2.3 ENGINEERING MODEL TELESCOPE PROTON CALIBRATION DATA BNL 9/12/78

Normal Incidence

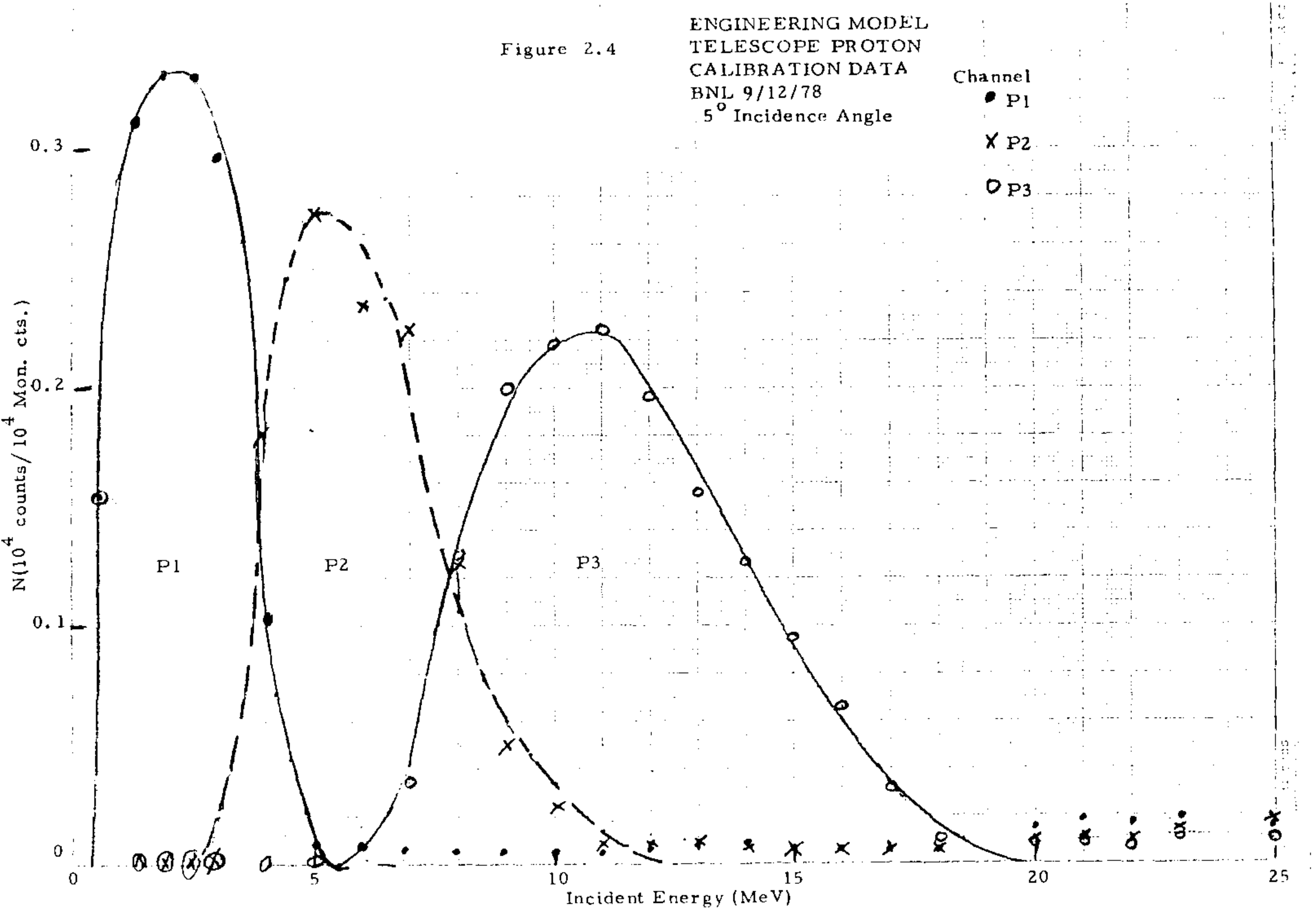

Figure 2.4

ENGINEERING MODEL
TELESCOPE PROTON
CALIBRATION DATA
BNL 9/12/78
5° Incidence Angle

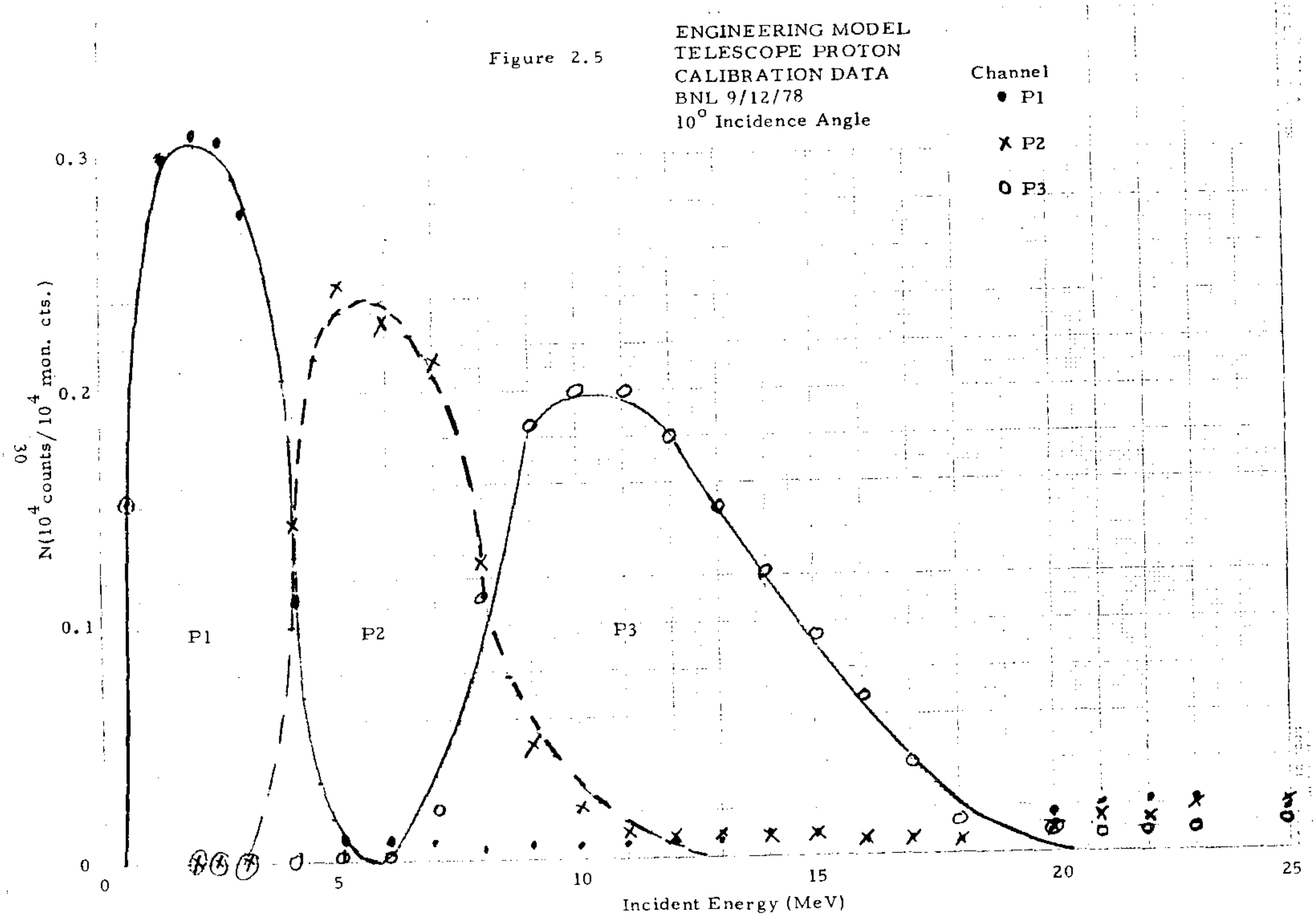

Figure 2.5

ENGINEERING MODEL
TELESCOPE PROTON
CALIBRATION DATA
BNL 9/12/78
10° Incidence Angle

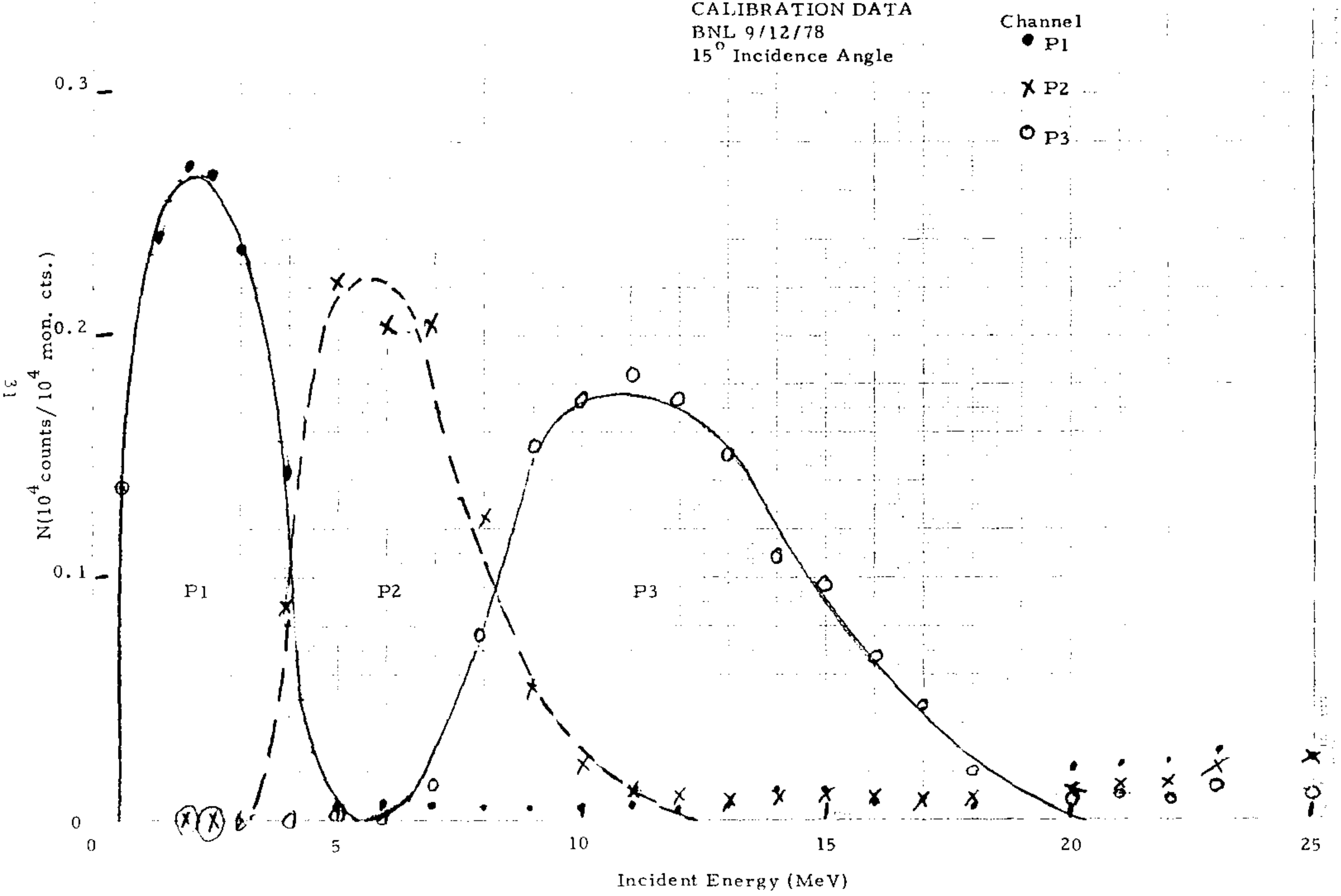

Figure 2.6 ENGINEERING MODEL TELESCOPE PROTON CALIBRATION DATA
BNL 9/12/78
15° Incidence Angle

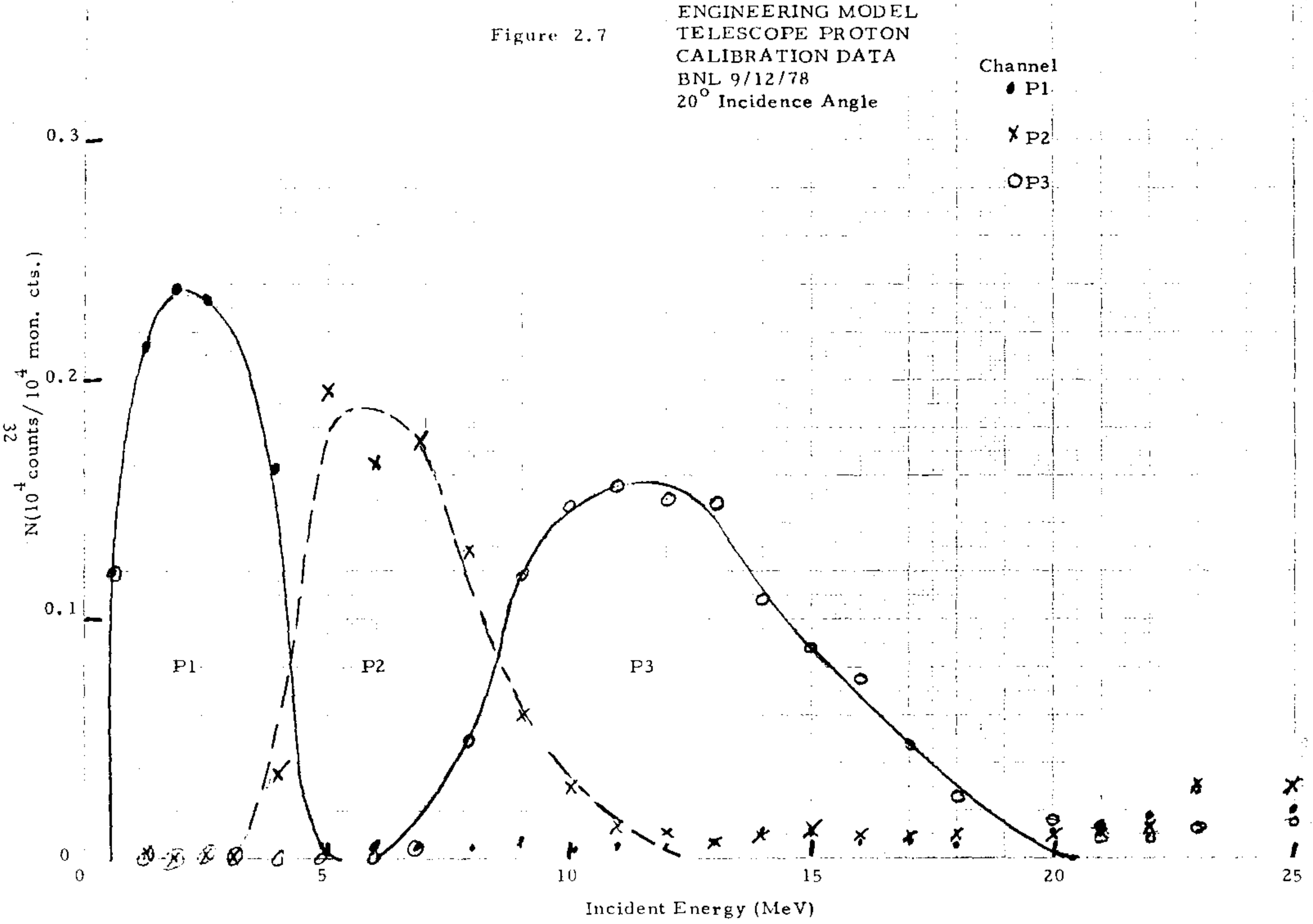

Figure 2.7

ENGINEERING MODEL
TELESCOPE PROTON
CALIBRATION DATA
BNL 9/12/78
20° Incidence Angle

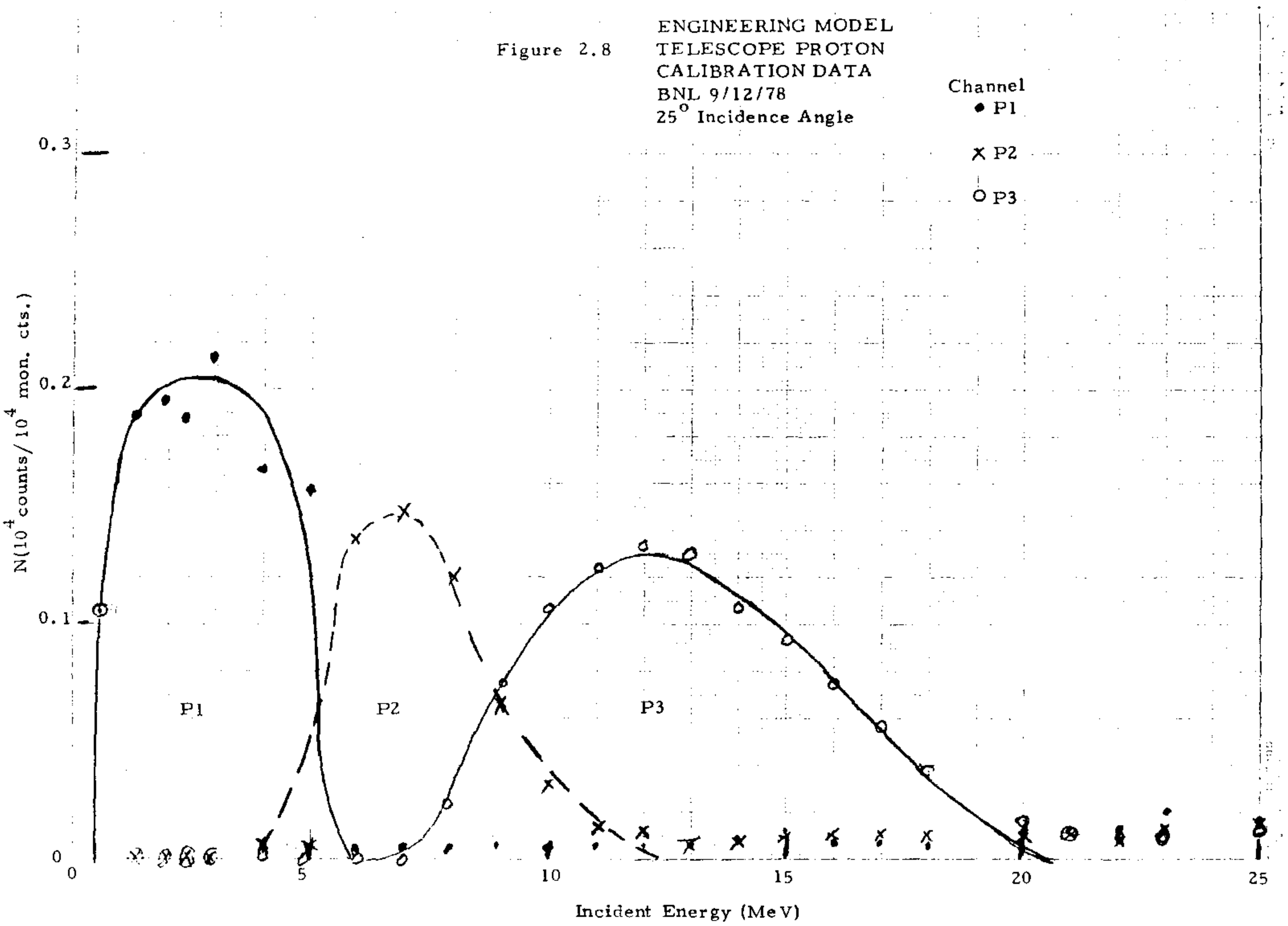

Figure 2.8 ENGINEERING MODEL TELESCOPE PROTON CALIBRATION DATA BNL 9/12/78 25° Incidence Angle

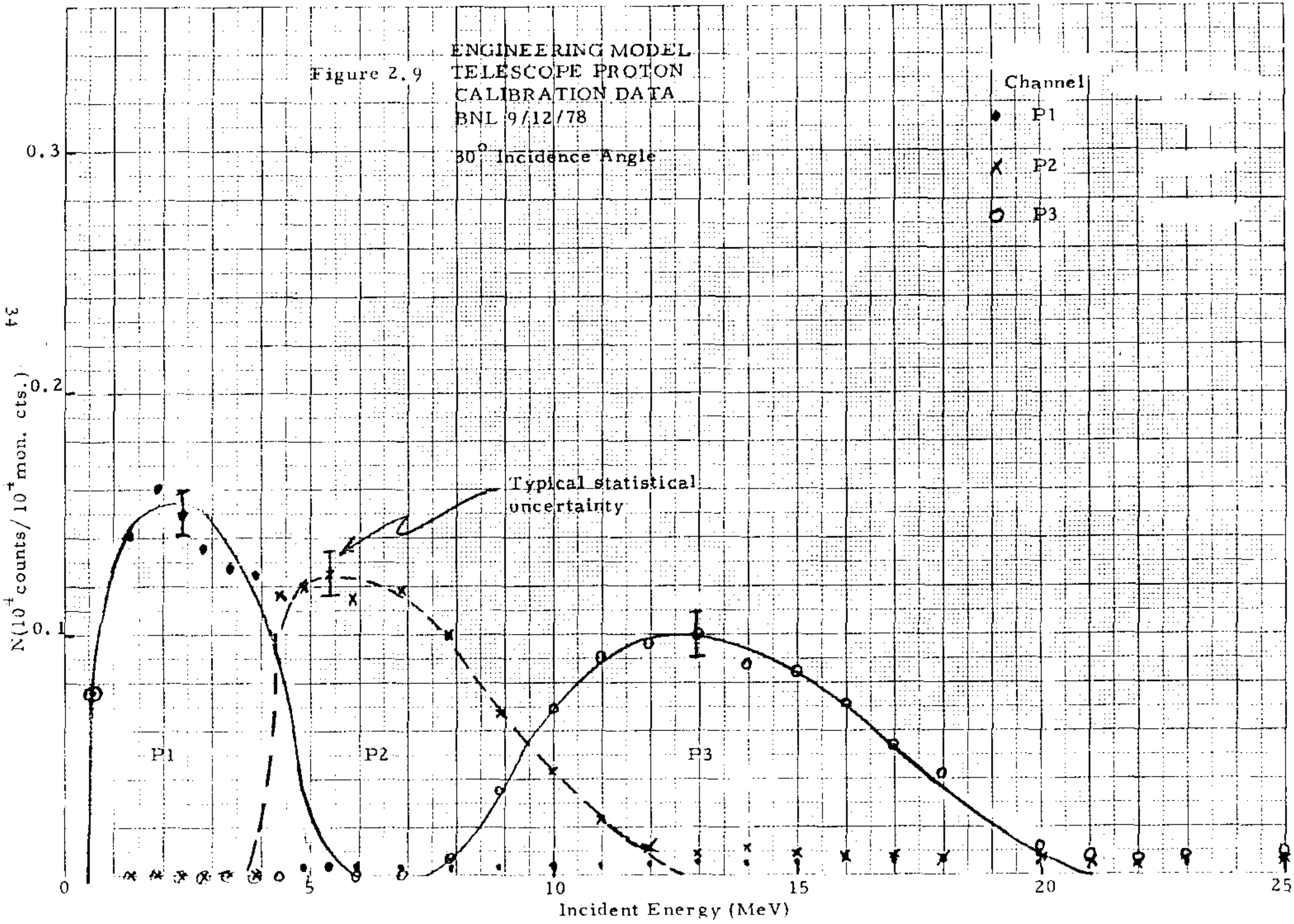

Figure 2.9 ENGINEERING MODEL TELESCOPE PROTON CALIBRATION DATA BNL 9/12/78

30° Incidence Angle

Typical statistical uncertainty

Figure 2.10 ENGINEERING MODEL
TELESCOPE PROTON
CALIBRATION DATA
BNL 9/12/78
35° Incidence Angle

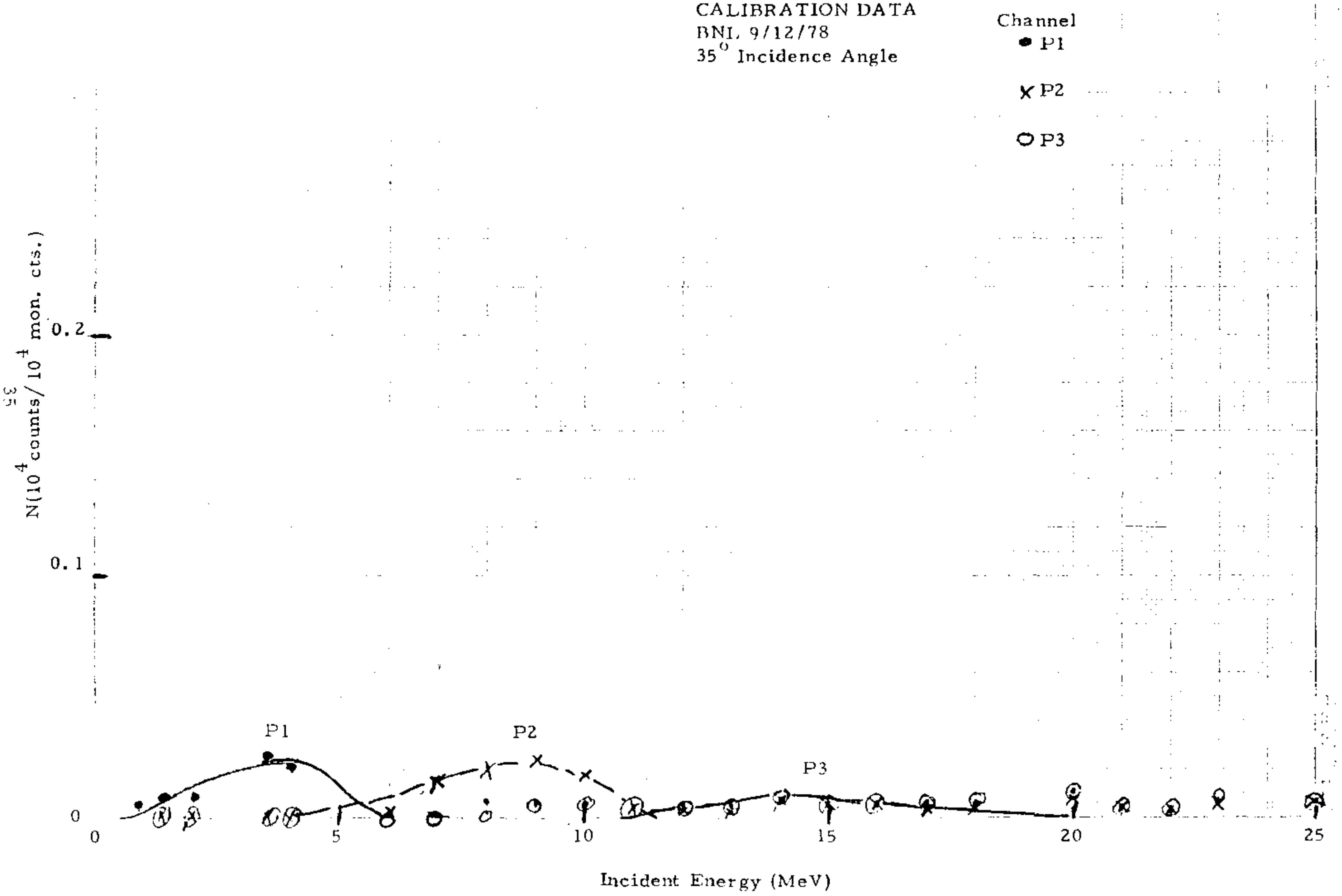

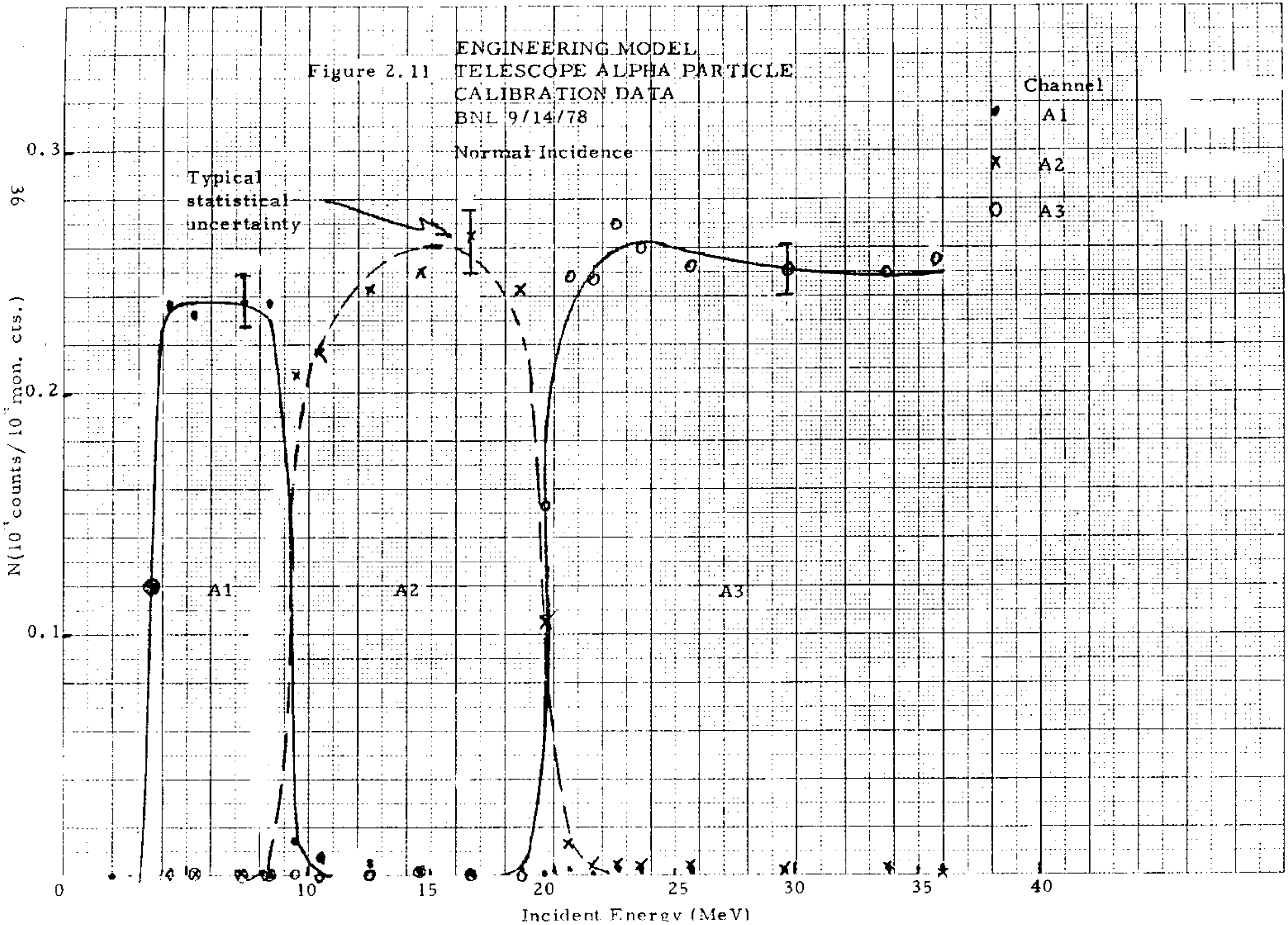

Figure 2.11 ENGINEERING MODEL TELESCOPE ALPHA PARTICLE CALIBRATION DATA BNL 9/14/78

Figure 2.12

ENGINEERING MODEL
TELESCOPE ALPHA PARTICLE
CALIBRATION DATA
BNL 9/14/78
5° Incidence Angle

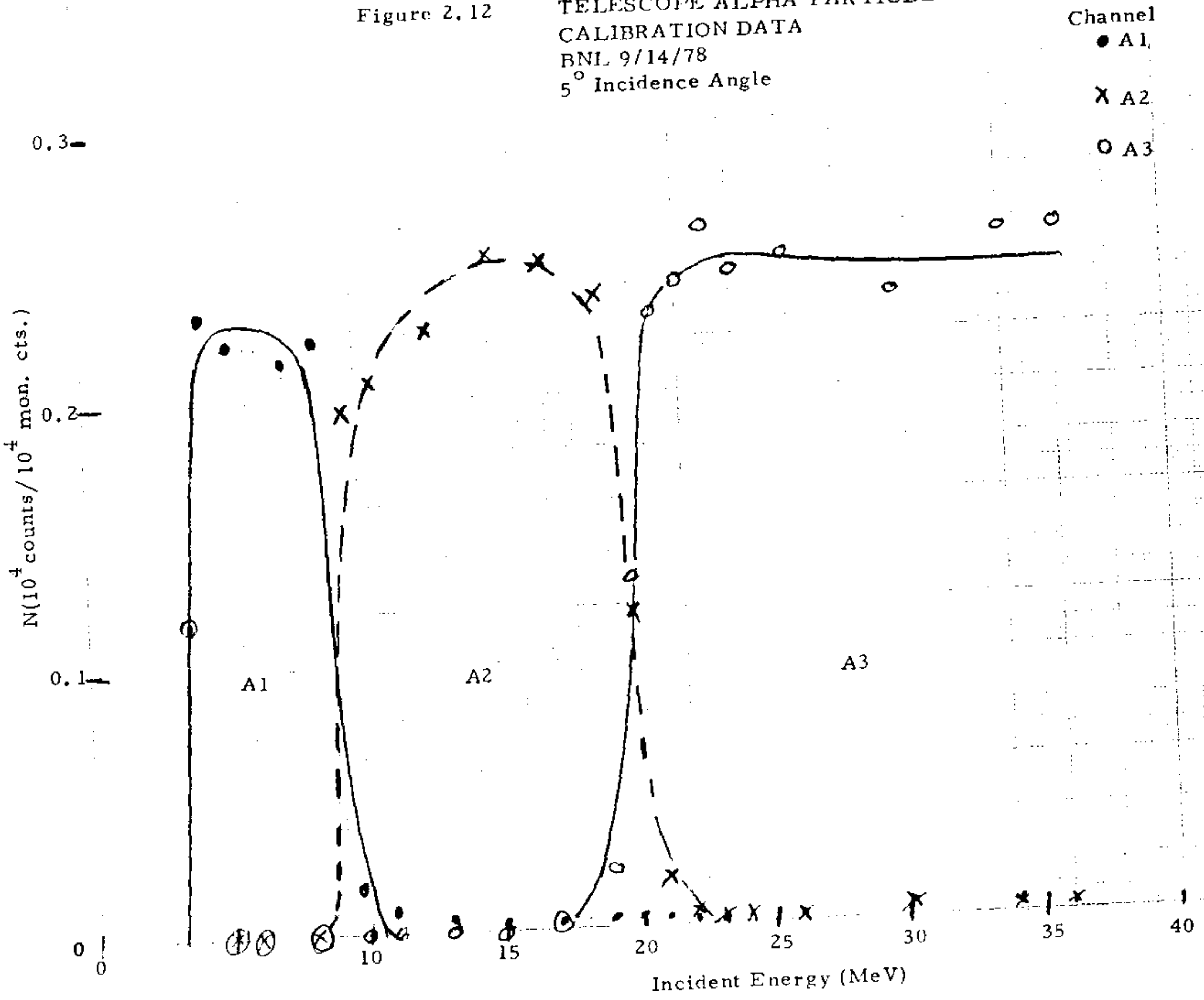

Figure 2.13 ENGINEERING MODEL TELESCOPE ALPHA PARTICLE CALIBRATION DATA
BNL 9/14/78
10° Incidence Angle

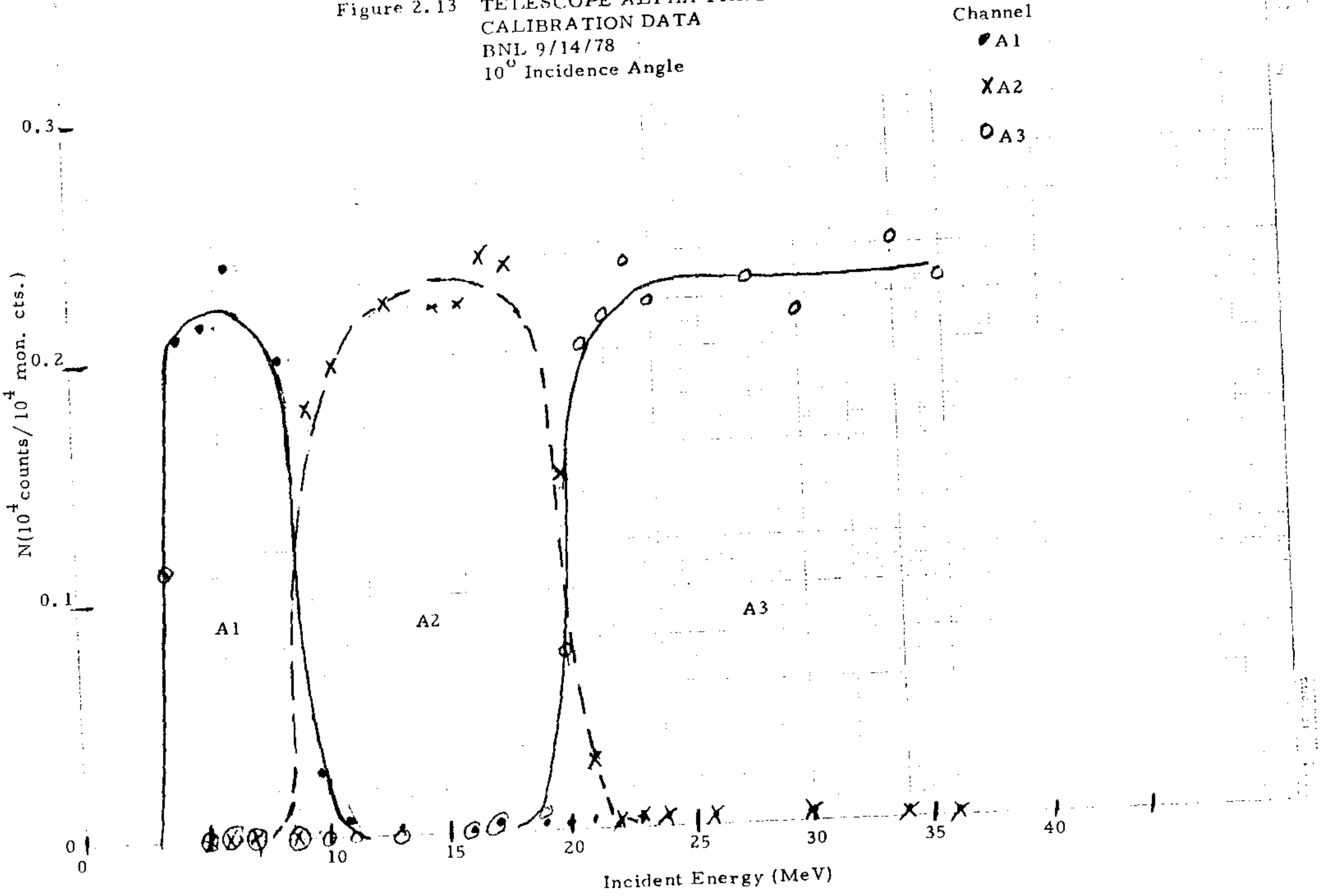

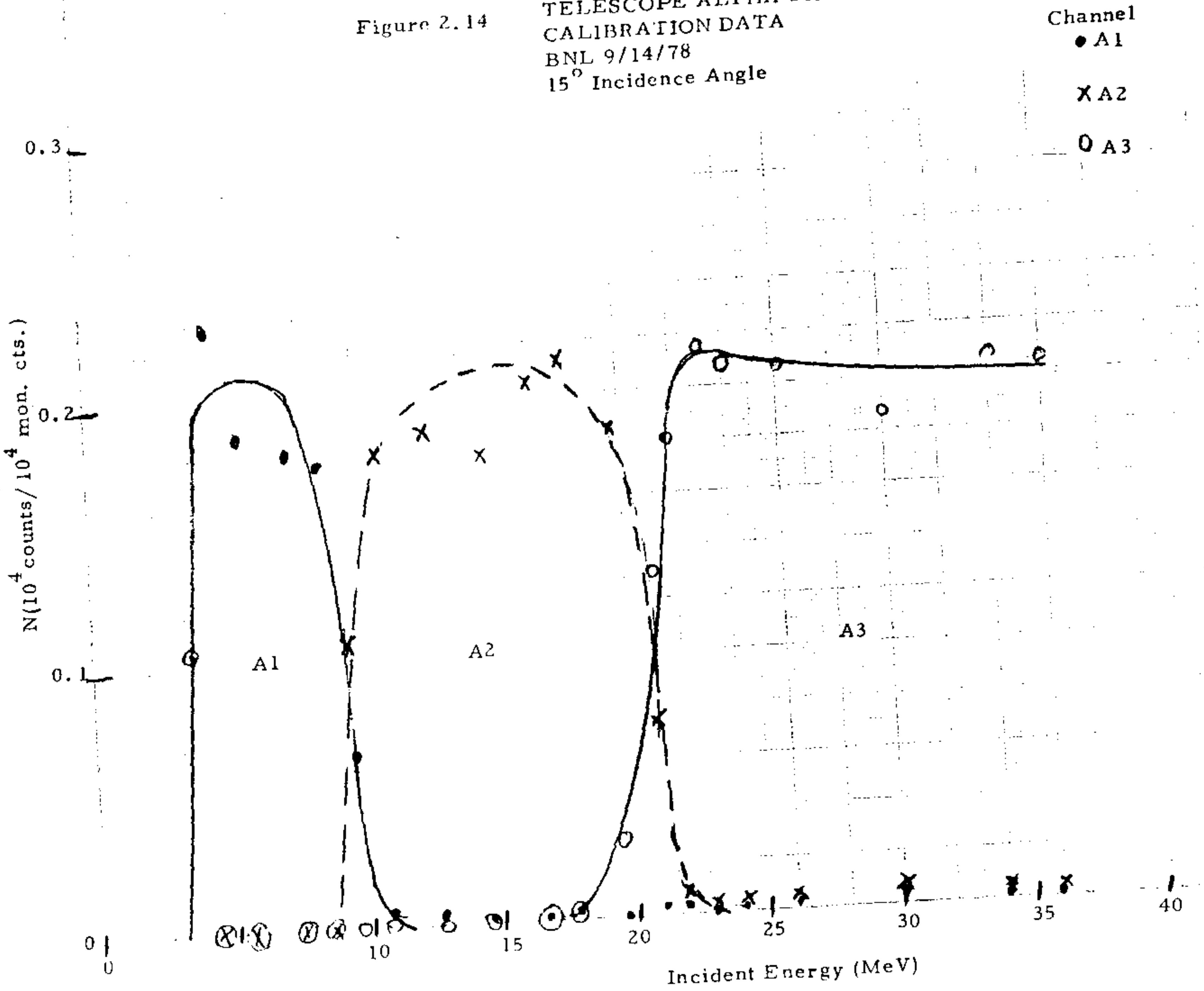

Figure 2.14

ENGINEERING MODEL
TELESCOPE ALPHA PARTICLE
CALIBRATION DATA
BNL 9/14/78
15° Incidence Angle

Figure 2.15 ENGINEERING MODEL
TELESCOPE ALPHA PARTICLE
CALIBRATION DATA
BNL 9/14/78
20° Incidence Angle

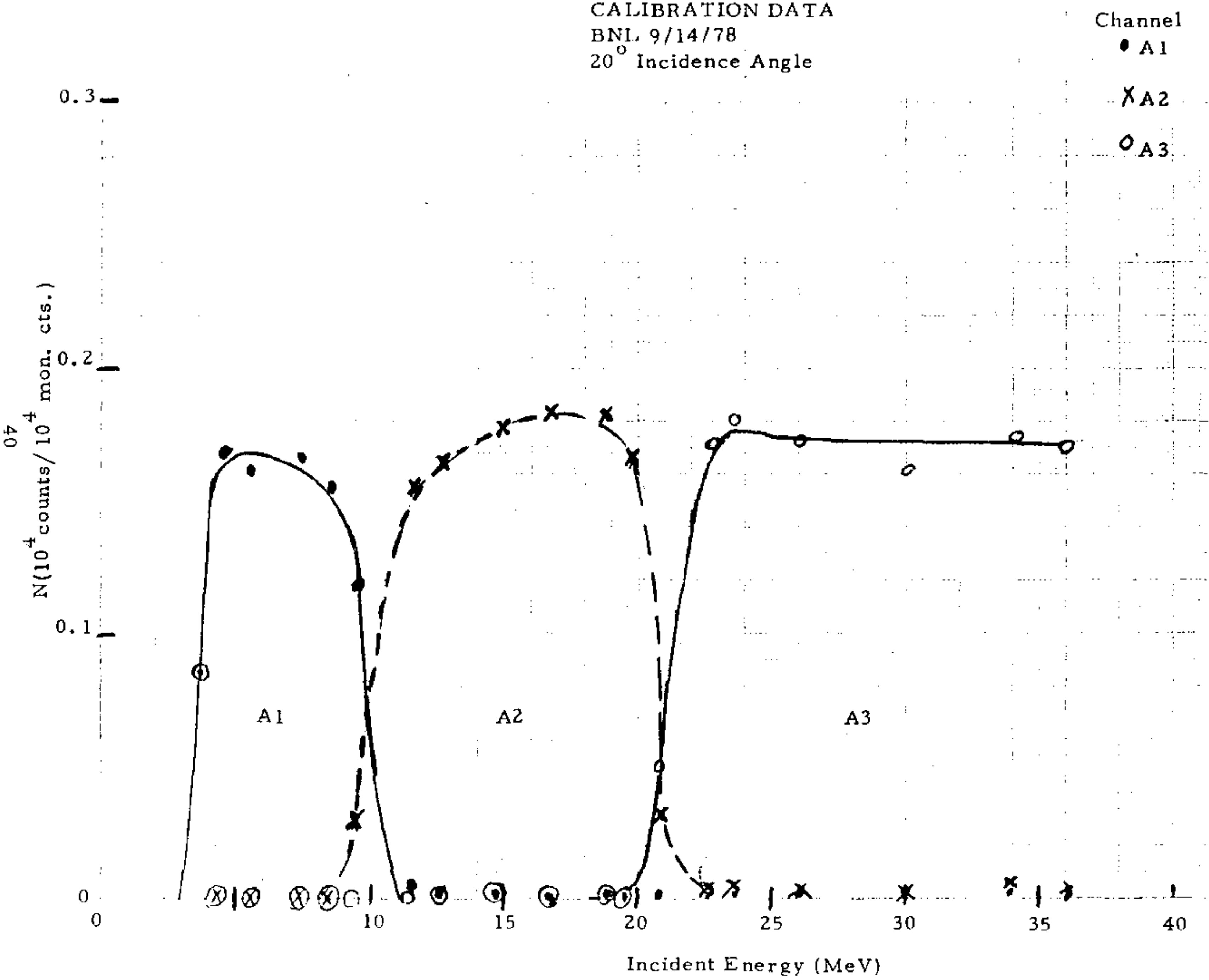

Figure 2.16 ENGINEERING MODEL
TELESCOPE ALPHA PARTICLE
CALIBRATION DATA
BNL 9/14/78
25° Incidence Angle

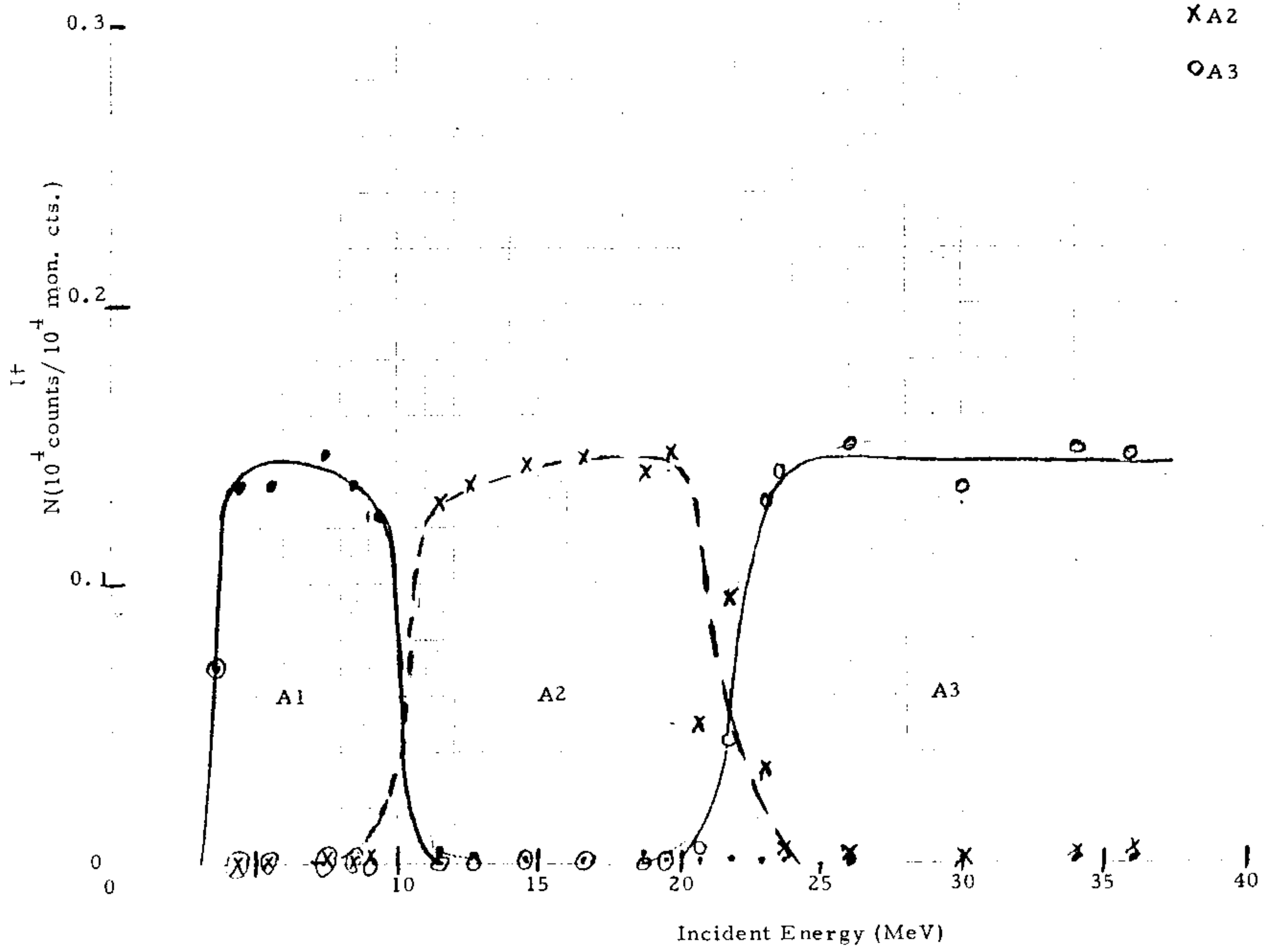

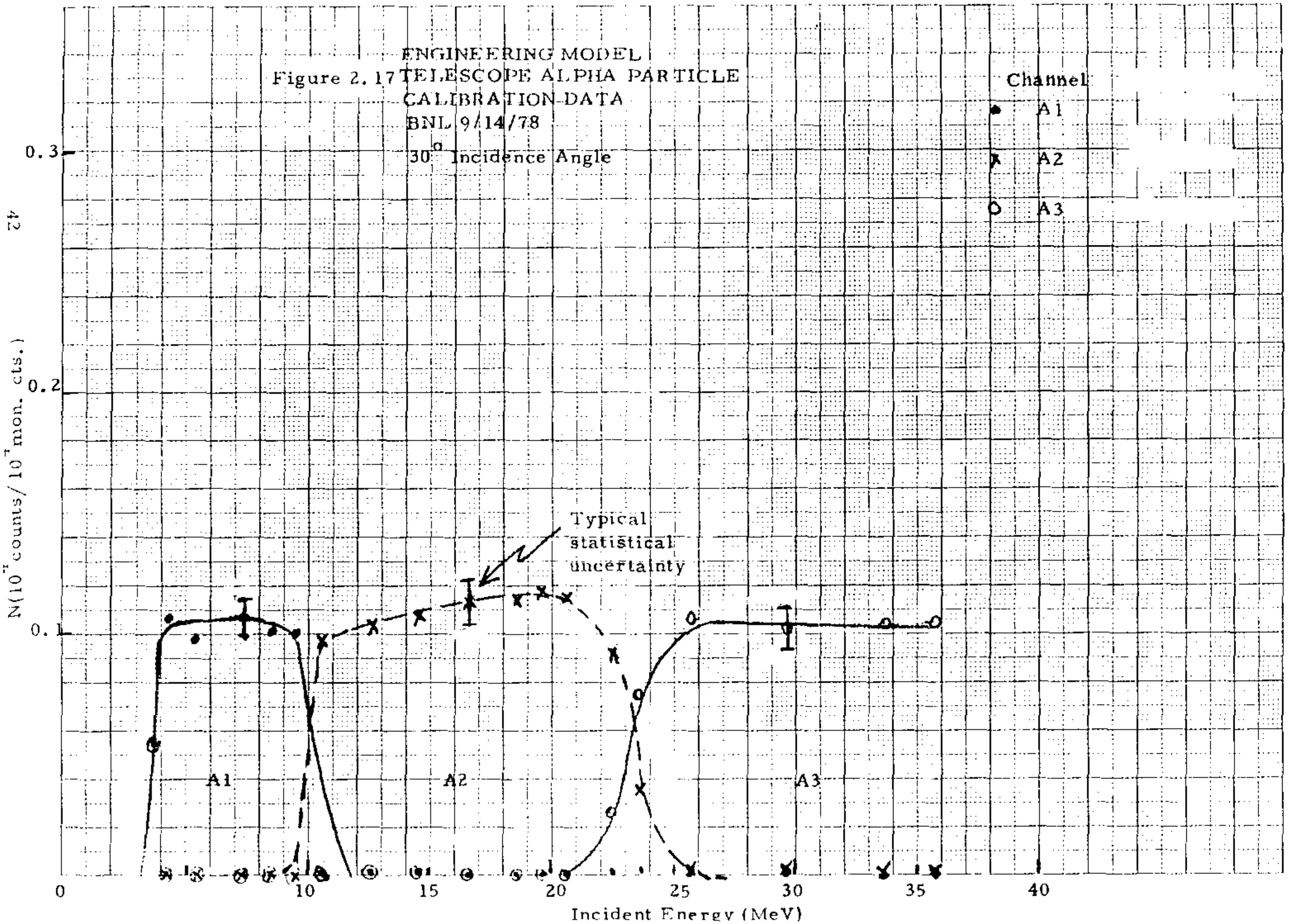

Figure 2.17 ENGINEERING MODEL TELESCOPE ALPHA PARTICLE CALIBRATION DATA BNL 9/14/78

30° Incidence Angle

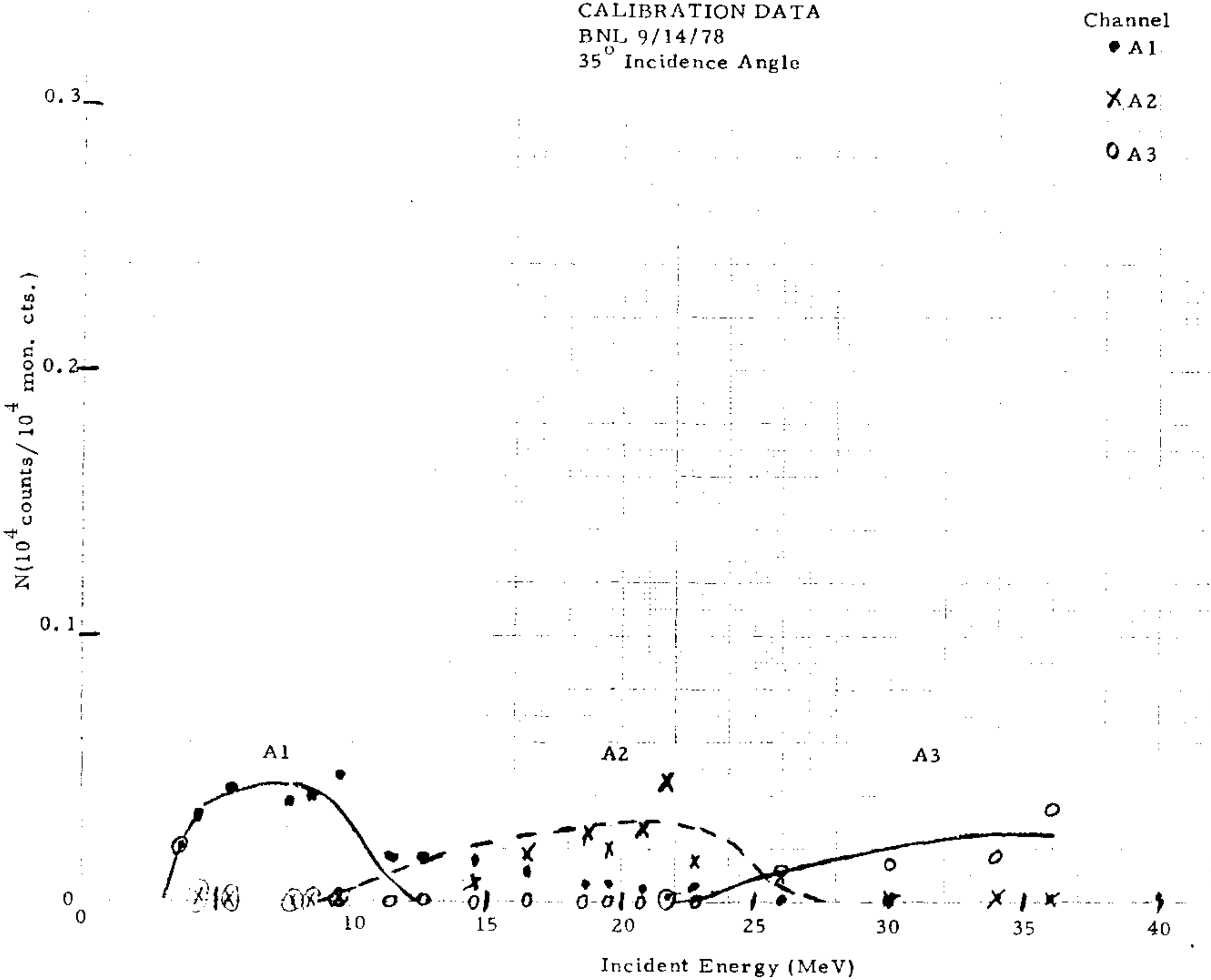

Figure 2.18 ENGINEERING MODEL TELESCOPE ALPHA PARTICLE CALIBRATION DATA BNL 9/14/78 35° Incidence Angle

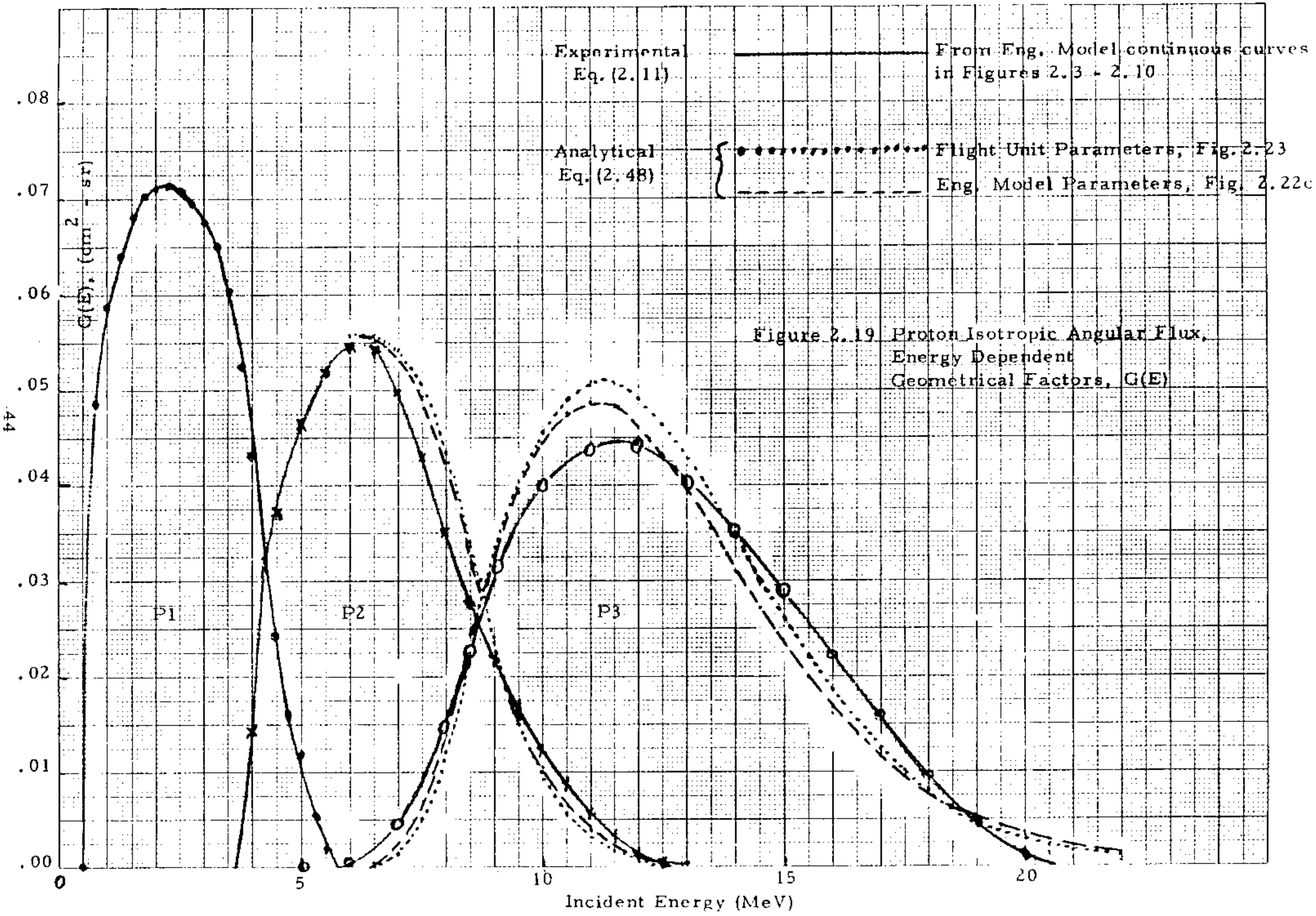

Figure 2.19 Proton Isotropic Angular Flux, Energy Dependent Geometrical Factors, G(E)

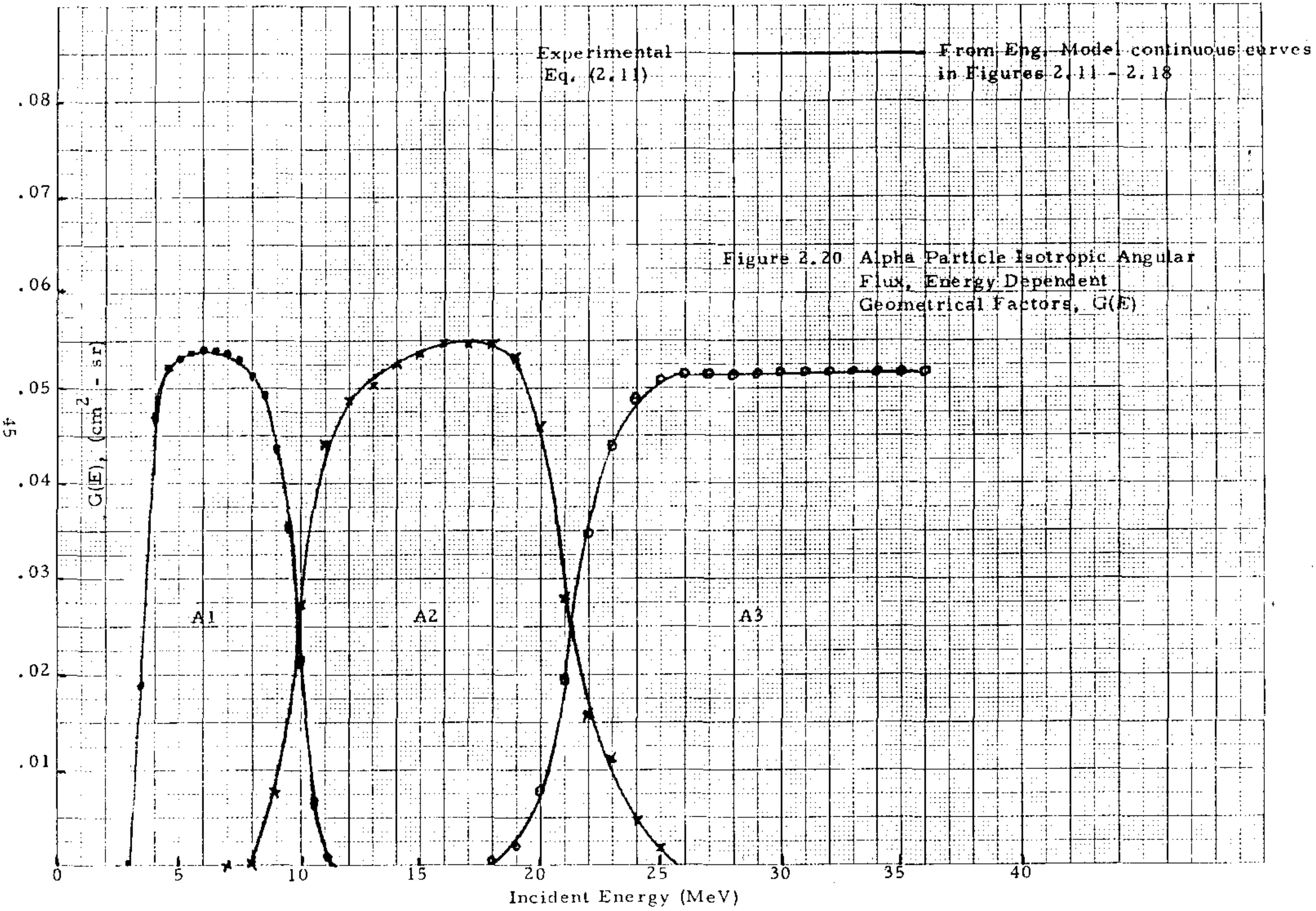

Figure 2.20 Alpha Particle Isotropic Angular Flux, Energy Dependent Geometrical Factors, G(E)

G(E). That expression gives the geometrical factor for any two energy pulse height limits E_1 and E_2. To find the value of G for any particular bin, these limits are set to the correct values for that bin. For numerical evaluation, the integral is replaced by a summation as follows:

$$G(E) = \sum_i g(E, \theta_i)\Delta\theta \tag{2.57}$$

where $\Delta\theta$, rad, is the width of the angular integration bins, and

$$g(E, \theta_i) = g_\infty(\theta_i) P(E_1, E_2, E, \theta_i) \text{ cm}^2 - \text{sr/rad} \tag{2.58}$$

is the "geometrical factor contribution" per radian at angle θ_i. Here, P is given by (2.28) and

$$g_\infty(\theta_i) = 2\pi A_{eff}(\theta_i) \sin\theta_i \cos\theta_i \tag{2.59}$$

with A_{eff} defined in (2.19). The reason this is labeled g_∞ is that it is the value of g obtained when the energy deposition pulse height limits become as wide as possible, i.e., $E_1 = 0$, $E_2 = E$, which yields from (2.29)

$$P(0, E, E, \theta_i) = 1 \tag{2.60}$$

Thus, g has its limiting value g_∞ in this case, and from (2.57) and (2.58), the maximum value of G is found to be

$$G_{max} = \sum_i g_\infty(\theta_i)\Delta\theta \quad \text{cm}^2 - \text{sr} \tag{2.61}$$

A FORTRAN program, given in Figure 2.21, has been written for determination of G(E) by use of Eq. (2.57). In addition to the energy deposition constants in Table 1.1, the program also requires as input data the type particle used ($T_o = Mc^2 = 938$ MeV and $z = 1$ for protons) and the detection system data in Table 2.2 below. The detector thicknesses are equivalent to those in Table 1.2, and the energy noise widths are the result of laboratory measurements with the indicated unit. The preamplifier is capable of better noise than is indicated, but due to power limitations, it was necessary to limit the input power somewhat, which degrades the performance. It is still completely acceptable due to the large value of threshold level 1 (Table 1.3) compared to the noise width.

TABLE 2.2

Detection System Input Data for Analytical G(E) Determination, Channel P3

Parameter	Eng. Model	Flight Units
Detector thickness, x, g/cm^2	0.01090	0.01165
Entrance Aperture Area (Fig. 2.1), $A = \pi r^2$, cm^2	0.0993	0.0993
$C \equiv h/(2r)$ (Fig. 2.1 and Eq. (2.20))	0.8929	0.8929
P3 Lower Pulse Height, E_1, MeV	0.310	0.325
P3 Upper Pulse Height, E_2, MeV	0.460	0.490
Energy Noise Width $\Delta E_n \equiv$ DEN, MeV	0.070	0.060

Figure 2.21 is a copy of the FORTRAN program, TELFAC, which calculates G(E), and Figures 2.22 and 2.23 are the output tabulations resulting from running the program for Bin P3 by use of the data in Tables 1.1 and 2.2. The numerical integration is carried out at $\Delta\theta = 1^\circ$ increments.

On the output tabulations, the particle energy is labeled T, rather than E as above, and the following additional identities are used:

THETA $\equiv \theta_i$

GITH $\equiv g_\infty(\theta_i)$, Eq. (2.59)

E0 $\equiv E_d$ (the energy deposited in detector, Sec. 1.3)

QP $\equiv Q'$, Eq. (2.45)

DELS $\equiv \Delta E_s$, Eq. (2.47)

EW $\equiv E_w$, Eq. (2.22)

FRAC $\equiv P(E_1, E_2, E, \theta)$, Eq. (2.29)

GTH $\equiv g(E, \theta_i)$, Eq. (2.58)

BSQ $\equiv \beta^2$, Eq. (2.32)

B $\equiv$ Stopping number, Eq. (2.44)

Q $\equiv q$, Eq. (2.43)

G $\equiv G(E)$, Eq. (2.57)

Figure 2.21 Program TELFAC for Calculation of Energy Dependent Geometrical Factor of Telescope

```
 COPY TTY:<FLP:TELFAC.FT
FILES COPIED:
TELFAC.FT
C          TELFAC.FT: G(E)FOR TELESCOPE,8/24/79
           COMMON Y,SEC
           DIMENSION Y(37),SEC(37)
 1         READ(1,101)X,A,C
           READ(1,102)E1,E2,DEN
           DTH=.01745
           G=0.
           DO 5 I=1,37
           TH=FLOAT(I)*DTH-.008725
           SEC(I)=1./COS(TH)
           U=C*TAN(TH)
           E0=SQRT(1.-U**2)
           E0=1.-.6366*(U*E0+ATAN(U/E0))
           U=6.2832*COS(TH)*SIN(TH)*E0*A
           TH=FLOAT(I)-.5
           IF(TH-35.)3,3,2
 2         U=U*(37.-TH)/2.
 3         Y(I)=U
           G=G+U*DTH
 5         CONTINUE
           WRITE(1,110)G
           READ(1,103)T0,ZZ,EN,EK,EPS
           DS=1./(EK*EN)
           V=EN-1.
           ENI=1./EN
           XK=X/EK
 10        READ(1,104)ES,DE,EF,L
           IF(L-1)14,12,12
 12        WRITE(1,108)
           DO 13 I=1,37
           TH=FLOAT(I)-.5
 13        WRITE(1,109)I,TH,SEC(I),Y(I)
 14        B0=6.532/ZZ**2
           D=.6567*ZZ*SQRT(X)
           H=DEN**2
           E=ES-DE
 15        E=E+DE
           U=E/T0
           B2=U*(U+2.)/(U+1.)**2
           S=DS*(E+EPS)**(-V)
           P=P0*B2*S
           W=-.59*(ALOG(.5577*D))**.4114
           G=0.
           IF(L-1)25,20,20
 20        WRITE(1,105)
 25        DO 80 I=1,37
           E0=S*X*SEC(I)
           U=1.-E0/E
           IF(U-.001)28,28,26
 26        E0=E+EPS
           E0=E0-(E0**EN-XK*SEC(I))**ENI
 28        OP=(1.-E0/E)**W
```

Figure 2.21 (Continued)

```
      IF(B2-.0075)30,35,35
30    C=(.00186/B2)*ALOG(102.*B2+.746)
      GO TO 40
35    C=(.0009/B2)*ALOG(306.*B2)
40    EW=(1.-.5*B2)/(1.-B2)
      DES=D*SQRT(SEC(I)*EW*(1.+Q)*QP)
      EW=.601*SQRT(H+DES**2)
      M=1
      F=(E1-E0)/EW
      GO TO 70
45    EP1=EPF
      M=2
      F=(E2-E0)/EW
      GO TO 70
50    EP1=EPF-EP1
      M=3
      F=E0/EW
      GO TO 70
55    EP2=EPF
      M=4
      F=(E-E0)/EW
      GO TO 70
58    F=EP1/(EP2+EPF)
      GTH=F*Y(I)
      G=G+GTH*DTH
      IF(L-1)80,60,60
60    TH=FLOAT(I)-.5
      WRITE(1,106)TH,E0,QP,DES,EW,F,GTH
      GO TO 80
70    EPF=1.
      IF(F)71,75,71
71    Z=ABS(F)
      IF(Z-9.)72,75,75
72 .  TP=1./(1.+.3275911*Z)
      U=.254829592*TP-.284496736*TP**2+1.42141374*TP**3
      U=U-1.453152027*TP**4+1.061405429*TP**5
      EPF=-Z*Z
      EPF=(1.-U*EXP(EPF))*F/Z
75    GO TO(45,50,55,58)M
80    CONTINUE
      WRITE(1,107)E,B2,B,Q,G
      IF(E-EF)15,10,10
101   FORMAT('  X='F7.5/'  A='F7.5/'  C='F7.5)
102   FORMAT(' E1='F5.2/' E2='F5.2/'DEN='F5.3)
103   FORMAT(' T0='F5.0/'  Z='F2.0/'  N='F6.3/'  K='F10.7/'EPS='F5.3)
104   FORMAT(' ES='F4.1/' DE='F4.1/' EF='F4.1/'  L='I2)
105   FORMAT(//'  THETA   E0      QP      DELS     EW      FRAC    GTH')

106   FORMAT(F6.1,6F8.4)
107   FORMAT('T='F5.1,'  BSQ='F7.5,'  B='F6.2,'  Q='F6.3,'  G='F6.4)
108   FORMAT('  I   THETA  SECANT    GITH')
109   FORMAT(I3,F7.1,2F9.4)
110   FORMAT(//'GMAX='F6.4)
      END
```

Figure 2.22 Results of TELFAC Run for Protons, Channel P3, Engineering Model

```
.F TELFAC

  X=.0109
  A=.0993
   C=.8929
 E1=.31
 E2=.46
LEN=.07
```

Figure 2.22 a Variation of $g_{\infty}(\theta)$ With θ

```
GMAX=0.0557
 T0=938.
  Z=1.
  N=1.795
  K=.002508
EPS=.353
 ES=8.
 DE=2.
 EF=8.
  L=1
  I    THETA   SECANT    GITH
  1     0.5    1.0000   0.0054
  2     1.5    1.0003   0.0158
  3     2.5    1.0010   0.0258
  4     3.5    1.0019   0.0354
  5     4.5    1.0031   0.0444
  6     5.5    1.0046   0.0530
  7     6.5    1.0065   0.0611
  8     7.5    1.0086   0.0687
  9     8.5    1.0111   0.0757
 10     9.5    1.0139   0.0823
 11    10.5    1.0170   0.0883
 12    11.5    1.0205   0.0938
 13    12.5    1.0243   0.0988
 14    13.5    1.0284   0.1033
 15    14.5    1.0329   0.1072
 16    15.5    1.0377   0.1105
 17    16.5    1.0429   0.1134
 18    17.5    1.0485   0.1156
 19    18.5    1.0545   0.1174
 20    19.5    1.0608   0.1186
 21    20.5    1.0676   0.1193
 22    21.5    1.0748   0.1195
 23    22.5    1.0824   0.1191
 24    23.5    1.0904   0.1183
 25    24.5    1.0989   0.1169
 26    25.5    1.1079   0.1151
 27    26.5    1.1174   0.1128
 28    27.5    1.1273   0.1100
 29    28.5    1.1378   0.1067
 30    29.5    1.1489   0.1031
 31    30.5    1.1605   0.0990
 32    31.5    1.1728   0.0945
 33    32.5    1.1856   0.0896
 34    33.5    1.1991   0.0845
 35    34.5    1.2133   0.0789
 36    35.5    1.2282   0.0549
 37    36.5    1.2439   0.0168
```

Figure 2.22 b Variation of $g(E, \theta)$ with θ for E = 8 MeV

```
THETA   E0      CP      DELS     EW      FFAC     GTH
 0.5  0.4579  1.0342  0.0730  0.0608  0.5190  0.0028
 1.5  0.4581  1.0343  0.0730  0.0608  0.5177  0.0082
 2.5  0.4583  1.0343  0.0731  0.0608  0.5150  0.0133
 3.5  0.4588  1.0343  0.0731  0.0608  0.5111  0.0181
 4.5  0.4594  1.0344  0.0731  0.0608  0.5058  0.0225
 5.5  0.4601  1.0344  0.0732  0.0609  0.4991  0.0265
 6.5  0.4609  1.0345  0.0733  0.0609  0.4911  0.0300
 7.5  0.4619  1.0346  0.0734  0.0609  0.4818  0.0331
 8.5  0.4631  1.0347  0.0734  0.0610  0.4711  0.0357
 9.5  0.4644  1.0348  0.0736  0.0610  0.4591  0.0378
10.5  0.4659  1.0349  0.0737  0.0611  0.4457  0.0394
11.5  0.4675  1.0350  0.0738  0.0611  0.4310  0.0404
12.5  0.4693  1.0351  0.0739  0.0612  0.4150  0.0410
13.5  0.4712  1.0353  0.0741  0.0613  0.3977  0.0411
14.5  0.4733  1.0355  0.0743  0.0613  0.3793  0.0406
15.5  0.4756  1.0356  0.0744  0.0614  0.3597  0.0398
16.5  0.4780  1.0358  0.0746  0.0615  0.3391  0.0384
17.5  0.4807  1.0360  0.0748  0.0616  0.3176  0.0367
18.5  0.4835  1.0363  0.0751  0.0617  0.2954  0.0347
19.5  0.4864  1.0365  0.0753  0.0618  0.2725  0.0323
20.5  0.4896  1.0367  0.0755  0.0619  0.2493  0.0297
21.5  0.4930  1.0370  0.0758  0.0620  0.2260  0.0270
22.5  0.4966  1.0373  0.0761  0.0621  0.2027  0.0241
23.5  0.5003  1.0376  0.0764  0.0623  0.1798  0.0213
24.5  0.5043  1.0379  0.0767  0.0624  0.1575  0.0184
25.5  0.5086  1.0382  0.0770  0.0625  0.1361  0.0157
26.5  0.5130  1.0386  0.0774  0.0627  0.1158  0.0131
27.5  0.5177  1.0390  0.0777  0.0629  0.0970  0.0107
28.5  0.5227  1.0394  0.0781  0.0630  0.0798  0.0085
29.5  0.5279  1.0398  0.0785  0.0632  0.0644  0.0066
30.5  0.5334  1.0402  0.0789  0.0634  0.0508  0.0050
31.5  0.5392  1.0407  0.0793  0.0636  0.0390  0.0037
32.5  0.5452  1.0412  0.0798  0.0638  0.0294  0.0026
33.5  0.5516  1.0417  0.0803  0.0640  0.0215  0.0018
34.5  0.5583  1.0422  0.0807  0.0642  0.0152  0.0012
35.5  0.5654  1.0428  0.0813  0.0645  0.0104  0.0006
36.5  0.5728  1.0434  0.0818  0.0647  0.0068  0.0001
T=   8.0   PSQ=0.01684   P=   4.52   Q=  0.088   C=0.0140
```

Figure 2.22 c Variation of G(E) with Energy for E = 8 to 22 MeV

```
 ES=8.
 DE=0.5
 EF=22.
  L=0
T=   8.0  BSQ=0.01684  B=   4.52   Q=  0.088   G=0.0140
T=   8.5  BSQ=0.01788  B=   4.58   Q=  0.086   G=0.0230
T=   9.0  BSQ=0.01892  B=   4.64   Q=  0.084   G=0.0319
T=   9.5  BSQ=0.01995  B=   4.70   Q=  0.082   G=0.0393
T=  10.0  BSQ=0.02099  B=   4.75   Q=  0.080   G=0.0445
T=  10.5  BSQ=0.02202  B=   4.80   Q=  0.078   G=0.0476
T=  11.0  BSQ=0.02305  B=   4.85   Q=  0.076   G=0.0486
T=  11.5  BSQ=0.02408  B=   4.89   Q=  0.075   G=0.0479
T=  12.0  BSQ=0.02510  B=   4.94   Q=  0.073   G=0.0459
T=  12.5  BSQ=0.02613  B=   4.98   Q=  0.072   G=0.0429
T=  13.0  BSQ=0.02715  B=   5.02   Q=  0.070   G=0.0393
T=  13.5  BSQ=0.02817  B=   5.06   Q=  0.069   G=0.0353
T=  14.0  BSQ=0.02920  B=   5.10   Q=  0.068   G=0.0312
T=  14.5  BSQ=0.03021  B=   5.13   Q=  0.066   G=0.0272
T=  15.0  BSQ=0.03123  B=   5.17   Q=  0.065   G=0.0234
T=  15.5  BSQ=0.03225  B=   5.20   Q=  0.064   G=0.0199
T=  16.0  BSQ=0.03326  B=   5.23   Q=  0.063   G=0.0168
T=  16.5  BSQ=0.03427  B=   5.27   Q=  0.062   G=0.0140
T=  17.0  BSQ=0.03529  B=   5.30   Q=  0.061   G=0.0117
T=  17.5  BSQ=0.03629  B=   5.33   Q=  0.060   G=0.0096
T=  18.0  BSQ=0.03730  B=   5.35   Q=  0.059   G=0.0079
T=  18.5  BSQ=0.03831  B=   5.38   Q=  0.058   G=0.0065
T=  19.0  BSQ=0.03931  B=   5.41   Q=  0.057   G=0.0053
T=  19.5  BSQ=0.04032  B=   5.44   Q=  0.056   G=0.0043
T=  20.0  BSQ=0.04132  B=   5.46   Q=  0.055   G=0.0035
T=  20.5  BSQ=0.04232  B=   5.49   Q=  0.054   G=0.0029
T=  21.0  BSQ=0.04332  B=   5.51   Q=  0.054   G=0.0023
T=  21.5  BSQ=0.04431  B=   5.54   Q=  0.053   G=0.0019
T=  22.0  BSQ=0.04531  B=   5.56   Q=  0.052   G=0.0015
 ES=↑C
.
```

Figure 2.23 Results of TELFAC Run for Protons, Channel P3, Flight Units: Variation of G(E) with Energy for E = 6.5 to 22 MeV.

```
.R TELFAC
  X=.01165
  A=.0993
  C=.8929
 E1=.325
 E2=.490
DEN=.06

GMAX=0.0557
 T0=938.
  Z=1.
  N=1.795
  K=.002508
EPS=.353
 ES=6.5
 DE=0.5
 EF=22.0
  L=0
T=   6.5   BSQ=0.01372  B=   4.31   Q= 0.094   G=0.0002
T=   7.0   BSQ=0.01476  B=   4.38   Q= 0.092   G=0.0013
T=   7.5   BSQ=0.01580  B=   4.45   Q= 0.090   G=0.0051
T=   8.0   BSQ=0.01684  B=   4.52   Q= 0.088   G=0.0123
T=   8.5   BSQ=0.01788  B=   4.58   Q= 0.086   G=0.0218
T=   9.0   BSQ=0.01892  B=   4.64   Q= 0.084   G=0.0314
T=   9.5   BSQ=0.01995  B=   4.70   Q= 0.082   G=0.0396
T=  10.0   BSQ=0.02099  B=   4.75   Q= 0.080   G=0.0455
T=  10.5   BSQ=0.02202  B=   4.80   Q= 0.078   G=0.0492
T=  11.0   BSQ=0.02305  B=   4.85   Q= 0.076   G=0.0508
T=  11.5   BSQ=0.02408  B=   4.89   Q= 0.075   G=0.0506
T=  12.0   BSQ=0.02510  B=   4.94   Q= 0.073   G=0.0491
T=  12.5   BSQ=0.02613  B=   4.98   Q= 0.072   G=0.0465
T=  13.0   BSQ=0.02715  B=   5.02   Q= 0.070   G=0.0430
T=  13.5   BSQ=0.02817  B=   5.06   Q= 0.069   G=0.0389
T=  14.0   BSQ=0.02920  B=   5.10   Q= 0.068   G=0.0346
T=  14.5   BSQ=0.03021  B=   5.13   Q= 0.066   G=0.0302
T=  15.0   BSQ=0.03123  B=   5.17   Q= 0.065   G=0.0260
T=  15.5   BSQ=0.03225  B=   5.20   Q= 0.064   G=0.0221
T=  16.0   BSQ=0.03326  B=   5.23   Q= 0.063   G=0.0185
T=  16.5   BSQ=0.03427  B=   5.27   Q= 0.062   G=0.0154
T=  17.0   BSQ=0.03529  B=   5.30   Q= 0.061   G=0.0126
T=  17.5   BSQ=0.03629  B=   5.33   Q= 0.060   G=0.0103
T=  18.0   BSQ=0.03730  B=   5.35   Q= 0.059   G=0.0083
T=  18.5   BSQ=0.03831  B=   5.38   Q= 0.058   G=0.0067
T=  19.0   BSQ=0.03931  B=   5.41   Q= 0.057   G=0.0054
T=  19.5   BSQ=0.04032  B=   5.44   Q= 0.056   G=0.0043
T=  20.0   BSQ=0.04132  B=   5.46   Q= 0.055   G=0.0034
T=  20.5   BSQ=0.04232  B=   5.49   Q= 0.054   G=0.0027
T=  21.0   BSQ=0.04332  B=   5.51   Q= 0.054   G=0.0022
T=  21.5   BSQ=0.04431  B=   5.54   Q= 0.053   G=0.0017
T=  22.0   BSQ=0.04531  B=   5.56   Q= 0.052   G=0.0014
 ES=0
```

As shown in Figure 2.22 a, the program first tabulates $g_{\infty}(\theta)$ over the range 0 to 37° at 1° increments. This simply shows the effects of the detection system geometry. Without the effect of P, the region near 22° contributes most significantly to G(E). The maximum value of G is given, and it is

$$G_{max} = 0.0557 \text{ cm}^2 - \text{sr} \tag{2.62}$$

The program then allows an option of tabulating the variation of $g(E, \theta)$ with θ for each energy, or of simply tabulating G(E) vs. E. Figure 2.22 b shows the tabulation of $g(E, \theta)$ for $E = 8$ MeV. Here, it is seen that the maximum contribution to G(E) comes from the region 12 - 13°. This is caused by the variation of energy deposition, and, hence, the probability P, with E. For particle energies nearer the center of the energy channel, $g(E, \theta)$ peaks nearer that of $g_{\infty}(\theta)$. In general, it is found that $\theta = 20°$ is a reasonable angle to use as an "average" angle of incidence for purposes of approximate energy channel definitions. Note also that the energy straggling width ΔE_s is about .07 - .08 MeV. Hence, this effect contributes about as much to the observed pulse distribution width as does the noise, ΔE_n.

It is interesting to note that $\overline{G}(E)$, defined by Eq. (2.53) for a given channel, will generally yield a result that is very close to the analytical maximum in Eq. (2.61). This is because the effects of ΔE_n and ΔE_s on G(E) are simply to increase its value outside the $\Delta E = E_{2i} - E_{1i}$ limits by the same amount that it is decreased within the limits. Thus, the integral over all energy must yield the same result as if these spreading effects did not exist.

Figure 2.22 c and Figure 2.23 show the variation of G(E) with energy for the engineering model and flight units, respectively. These are the results that are plotted in Figure 2.19 for channel P3. Also shown there are calculations made for the response near level 2 for channel P2.

In general, there are two important observations to be made regarding the results in Figure 2.19:

1) The two analytical results are quite close to each other, showing that there is little difference between the engineering model and flight unit responses. This is because the energy deposition thresholds (Table 1.3) were adjusted to take into account the small differences in detector thicknesses (Table 1.2).

2) The analytical and experimental results agree reasonably well with each other. There are several degrees of approximation in calculation of the energy loss straggling. The simplest is the Gaussian approximation used above. The next simplest approximation does take into account some possible asymmetry in the energy loss distribution (Ref. 2.1), but requires an additional numerical integral. This was actually done here for several energies, but the

difference was only marginally significant. The difference between the analytical and experimental results in Figure 2.19 appears, in our judgment, to be slightly outside the experimental uncertainty of the measurements. A completely detailed calculation of the straggling effects could perhaps improve the agreement, but it is not warranted for present purposes.

From the agreement of analytical calculations with each other, and the fact that the results also agree reasonably well with experiment, we conclude that (1) the observed, rather broad, response in P3 is correct, and (2) the engineering model experimental G(E) values can be used for the flight units.

We believe that it was necessary to carry out the analytical calculations in order to prove these two important conclusions.

2.2.2 Channel Average Geometrical Factor

Following the procedure in Section 2.1.4, we have integrated the experimental results in Figures 2.19 and 2.20 in accord with Eq. (2.53). The results are given in Table 2.3.

TABLE 2.3

Experimental Values of Channel Average Geometrical Factors

Channel	E1i (MeV)	E2i (MeV)	ΔE (MeV)	$\overline{E}$ (MeV)	$\overline{G}(E)$(cm^2-sr)
P1	0.6	4.2	3.6	2.4	.0665
P2	4.2	8.7	4.5	6.5	.0536
P3	8.7	14.5	5.8	11.6	.0583
A1	3.8	9.9	6.1	6.9	.0534
A2	9.9	21.3	11.4	16.1	.0538
A3	21.3	61.0	39.7	41.2	.0515

The experimental data for channel A3 did not extend past 36 MeV. However, the shape of G(E) in the region where the channel begins to count (near E1i = 21.3), and the very flat response within the channel show that the average value, $\overline{G}(E)$, will be just the flat maximum value - hence, the result given for A3.

With the exception of channel P1, all of these results are within ±8% of the analytical maximum value of 0.0557 cm^2 - sr, Eq. (2.62). As noted in

Section 2.2.1.2, this is to be expected. The only result that is not within this limit is channel P1. A discussion of possible reasons for this channel $\overline{G}(E)$ being too high has been given in Section 2.2.1.1. We cannot, however, state with certainty that any particular experimental problem caused this effect. Nevertheless, we know no reason that it should be higher than the analytical maximum; and our best judgment is that the correct value is nearer 0.056 cm^2 - sr.

It is our conclusion that all of the values of $\overline{G}(E)$ should be taken as 0.056 cm^2 - sr within the experimental uncertainties. Furthermore, if the values of G(E) in Figures 2.19 and 2.20 are to be used, they should probably be normalized in such a way that each resulting $\overline{G}(E)$ will have the value 0.056 cm^2 - sr, rather than the results given in Table 2.3. This is a very small effect in all cases except for channel P1.

3. SPURIOUS GEOMETRICAL FACTOR DETERMINATION

3.1 Method of Approach

The only significant spurious effects expected are due to very energetic protons that can penetrate the out-of-aperture shielding of the Telescope. Although all alpha channels are affected to a small degree by > 100 MeV protons, none are affected significantly by lower energies, except for a very narrow region near 90 MeV that affects A1.

The method of approach is to determine the results expected analytically, correlate these with the experimental data, and combine the two approaches to obtain the best estimate of the spurious geometrical factors. Because the problem is one of, essentially, finding the background effects in the primary channels, the detailed dependence G(E) of the geometrical factors is not needed and is not determined. Rather, it is the energy average geometrical factor, discussed in general in Section 2.1.4, that is appropriate and is determined in the following section.

3.2 Results

3.2.1 Analytical

Considering the coincidence mode of operation, the analytical approach proceeds as follows. The directions for the incident protons are split into small and large angles to the telescope axis for the front and rear entry. An examination of the detector shielding gives the approximate shielding and other factors as listed below in Table 3.1..

TABLE 3.1

Approximate Shielding and Maximum Possible Geometrical Factors

Direction of incidence	Angular range(deg)	Shielding Thickness* W equivalent(g/cm^2)	Approx. $G_{max}(cm^2\text{-}sr)$	Effective detector Thicknesses** First/Second (F=front, R=rear)
Front (1)	0 - 45	6	1.6	58.6(F)/586. (R)
Front (2)	45 - 75	15	0.7	100 (F)/1,000 (R)
Rear (2)	105 - 135	20	0.7	1,000 (R)/100 (F)
Rear (1)	135 - 180	10	1.6	586 (R)/58.6 (F)

*W ≡ tungsten

**Thicknesses in μm.

The above parameters were then used to calculate direct proton detection ranges, ΔE_d. The procedure was similar to that in Section 1.3, except that energy loss parameters for tungsten were used. Note that the rear entry particles have a larger amount of shielding to account for electronics, spacecraft, etc., shielding. The direct proton detection ranges for each proton channel are listed below in Table 3.2, along with the total $G_{max}\Delta E_d$. The values of $G_{max}\Delta E_d$ are obtained summing the products of the G_{max} values in Table 3.1 with the appropriate energy detection ranges, ΔE_d, shown.

TABLE 3.2

Values of $G_{max}\Delta E_d$

Proton Channel	Energy detection ranges (in MeV) for Front(1)	Front(2)	Rear(2)	Rear(1)	Total $G_{max}\Delta E_d$ $(cm^2\text{-}sr\text{-}MeV)$
P1	56.55-56.98	96.86-97.25	---	---- 116.18-116.31	0.96
P2	56.98-58.55	97.25-101.07	77.62-79.13	116.35-119.75	10.1
			77.61-77.62	116.12-116.18	
P3	58.55-61.03	101.07-106.31	79.13-80.80	119.75-124.26	13.5

The actual telescope shielding varies significantly with direction; therefore, the total $G_{max}\Delta E_d$ above was assigned to a total energy bin width ΔE covering the entire range of calculated energies. The $\overline{G}$ values given below were obtained by dividing the $G_{max}\Delta E_d$ values in Table 3.2 by the indicated values of ΔE.

TABLE 3.3

Analytical Results for Spurious Average Geometrical Factors

Proton Channel	Energy Range(MeV)	Channel Width ΔE (MeV)	Average Geometric Factor $\overline{G}$ (cm^2 - sr)	Average Area $\overline{A}$ (cm^2) (for $\Delta\Omega \simeq 9.3$sr)
P1	50 - 100	50	0.019	0.0021
P2	50 - 125	75	0.13	0.014
P3	60 - 125	65	0.21	0.022
A1	90 - 100	10	0.04	0.004

The average area $\overline{A}$ is calculated by dividing $\overline{G}$ by 9.3 sr, the approximate total solid angle ($\Delta\Omega$) of detection. The alpha particle channels have no proton detection, except for the single A1 channel, where 90 - 100 MeV protons at angles greater than 50 degrees can be detected and are shown in the table above. Protons below 50 MeV are effectively eliminated by shielding in all out-of-aperture directions, except for a small contribution from particles penetrating only part of the collimator edges. This is expected to be much smaller than the direct G factors and so is neglected.

3.2.2 Experimental Results

The proton beam measurements at the Harvard Cyclotron are summarized in the following Table 3.4.

TABLE 3.4

Experimental Measurements of G(E)

Proton Energy (MeV)	Incident Angle range** (degrees)	Partial G(E) (cm^2 - sr) for Channel* P1	P2	P3	A1	A2	A3
144	0 - 90	0.013	0.008	0.018	1.6-4	1.6-5	1.3-5
90	90 - 180	0.0048	0.036	0.036	All <5. - 4		
79	90 - 180	0.0018	0.034	0.026			
70	90 - 180	<6. - 4	0.0049	0.0036			
60	90 - 180	---	---	---			

*N - n $\equiv$ N x 10^{-n}

**Actual data have been extrapolated to allow calculation for an entire hemisphere.

The above results are integrated over the measurements made with front and rear irradiations, and each covers only half of a full 4π sr. If the 90 MeV results are doubled, they are about half of the theoretical values of $\overline{G}$ listed in Table 3.3. The measurements also show a weak sensitivity to very high energy protons, most likely due to nuclear reactions in the Si detectors.

3.2.3 Spurious Average Geometrical Factor

The above analytical and experimental results have been combined to give an estimate of the actual sensitivity of the telescope channels to high energy protons. The resulting $\overline{G}(E)$ factors, in (cm^2 - sr), are listed in Table 3.5 below.

TABLE 3.5

Spurious Average Geometrical Factors Summary

Channel	Proton Energy(MeV)	ΔE (MeV)	$\overline{G}(E)(cm^2$-sr)
P1	50 - 100	50	0.02
P1	> 100		0.02
P2	50 - 125	75	0.10
P2	> 125		0.02
P3	60 - 125	65	0.20
P3	> 125		0.04
A1	90 - 100	10	0.04
A1	> 100		0.0003
A2	> 100		0.0003
A3	> 100		0.0003

The above $\overline{G}(E)$ factors are estimated to be accurate to 50% and have been biased upward closer to the theoretical values. They should thus always indicate when high energy contamination is a likely problem.

Strictly, these results apply only for an isotropic angular flux. If the flux is non-isotropic, the angle-averaged flux should be used.

As discussed in Section 2.1.4, in order to define the average flux in a given channel by use of (2.55), it is necessary first to subtract the effects of spurious counts in the channel due to the response to energetic protons.

This is done for a given channel by summing the effects of the geometrical factors for each region, as defined in Table 3.5. Thus, the spurious count rate for channel n is

$$C_n = \sum_i \overline{F}_{ni}(E)\ \overline{G}_{ni}(E) \quad \text{cps} \tag{3.1}$$

where for a differential energy channel, the average flux $\overline{F}_{ni}$, $(\text{cm}^2\text{-sec-sr})^{-1}$, is

$$\overline{F}_{ni}(E) = \overline{f}_{ni}(E)\ \Delta E_{ni}, \tag{3.2}$$

with ΔE_{ni} MeV, the width of the channel, and $\overline{f}_{ni}(E)$, $(\text{cm}^2\text{-sec-sr-MeV})^{-1}$, the average angular differential flux. For an integral energy range in Table 3.5, $\overline{F}_{ni}(E)$ is simply the integral flux, $(\text{cm}^2\text{-sec-sr})^{-1}$, above the indicated energy.

Thus, to define the channel average flux by use of (2.55), the count rate (3.1) is subtracted from the observed count rate, and the values of $\overline{G}$ and ΔE from Table 2.3 are used for calculation of $\overline{f}(E)$. It should be noted that, although the values of $\overline{G}\Delta E$ for spurious counts are larger than the results for the primary radiation in Table 2.3, in general the count C_n will be much smaller than the observed count and will, in fact, represent only a correction. This is because the shape of solar proton spectra are such that the flux normally decreases rapidly with energy. A condition in which this is not true, however, can occur in the first few hours of a flare, when only the most energetic particles have had time to arrive. Effectively, the DOME data should be used to calculate the corrections C_n; and these should only be applied when they represent small corrections to the observed count rate, c.

4. SUMMARY AND CONCLUSIONS

4.1 Summary

Calibration Work on the previous GOES and SMS Telescope assemblies (Refs. 1.7-1.9) did not determine the angular dependence of the geometrical factors, although such effects were known to exist (Ref. 1.7, p. 5). Additionally, the maximum proton energy available at the Stanford accelerator, where the work was done, was about 16 MeV. Both of these deficiencies have been corrected in the present work: the in-aperture angular response was measured at the Brookhaven National Laboratory Van de Graaff Accelerator throughout the region 0 - 40° (response is zero at 40°), and the energy range was extended to at least 25 MeV for protons (Figures 2.3 - 2.10) and to 36 MeV for alpha particles (Figures 2.11 - 2.18).

The experimental data were integrated over angle assuming an isotropic flux to obtain the results for the energy dependent primary geometrical factor, G(E), for each particle channel, as shown in Figures 2.19 and 2.20. These results compare satisfactorily with a detailed, analytical approach. For convenience, it is sometimes assumed that the flux is, essentially, independent of energy within the immediate region of each energy channel. Under these conditions, it is possible to define the channel average geometrical factor, $\overline{G}(E)$, as in Section 2.1.4. The results are tabulated in Table 2.3, Section 2.2.2. As stated there, it is our judgment that the best value of $\overline{G}(E)$ to use is 0.056 cm^2-sr for all channels. The average flux is then defined by use of Eq. (2.55), the observed count rate, and the ΔE data in Table 2.3.

Corrections to the observed count rate must be made due to spurious counts produced by energetic protons ($\gtrsim$ 50 MeV) which are able to penetrate the shielding. Measurements made at the Harvard Cyclotron have been combined with analytical results to obtain the spurious average geometrical factors summarized in Table 3.5, Section 3. The method of correcting the observed counts for penetrating protons is discussed in that section.

4.2 Conclusions and Comparisons with Previous GOES Telescopes

Proton Calibration data taken at normal incidence are given in Figures 4.1 and 4.2 for SMS B and C (SMS 2 and GOES A in present nomenclature). The thresholds (Table 1, Ref. 1.8) were set at values similar to those used here, and the results shown in Figures 4.1 and 4.2 are consistent with the energy deposition diagram for the two detectors (Figure 4, Ref. 1.8), which is equivalent to Figure 1.2 here. The variation of G(E) for SMS B and C is generally very similar to the results here - compare with Figure 2.19, for example. The long "tails" on the distribution were probably due to particles penetrating the front detector (which must be mostly near its edge) and missing the back detector. This effect was completely eliminated in the present design (Figure 1.1) by utilizing tungsten collimators and by choosing the detector areas in such a way that any particle passing through the front detector must be incident on the back detector.

The design for GOES A was, apparently, changed in the direction to eliminate that problem, also. Response curves are given in Figure 4.3. In this instance, the tails in the response are attributed to anomalous beam-induced counts in the monitor detector (Ref. 1.9, p. 20). The "peaks" correspond to changes in the monitor detector threshold energy.

Comparision of Figure 2.3, taken for normal incidence, with Figure 4.3, shows the following. The response characteristics in the P1 and P2 channels are not greatly different, although the rate of change with energy near the channel edges is probably somewhat more rapid for GOES C. This suggests that the noise width ΔE_n of the GOES C preamplifier is lower than the .060 MeV for the present Telescope. As noted earlier, this noise figure is the result of operating the preamplifier at a low input power level. It

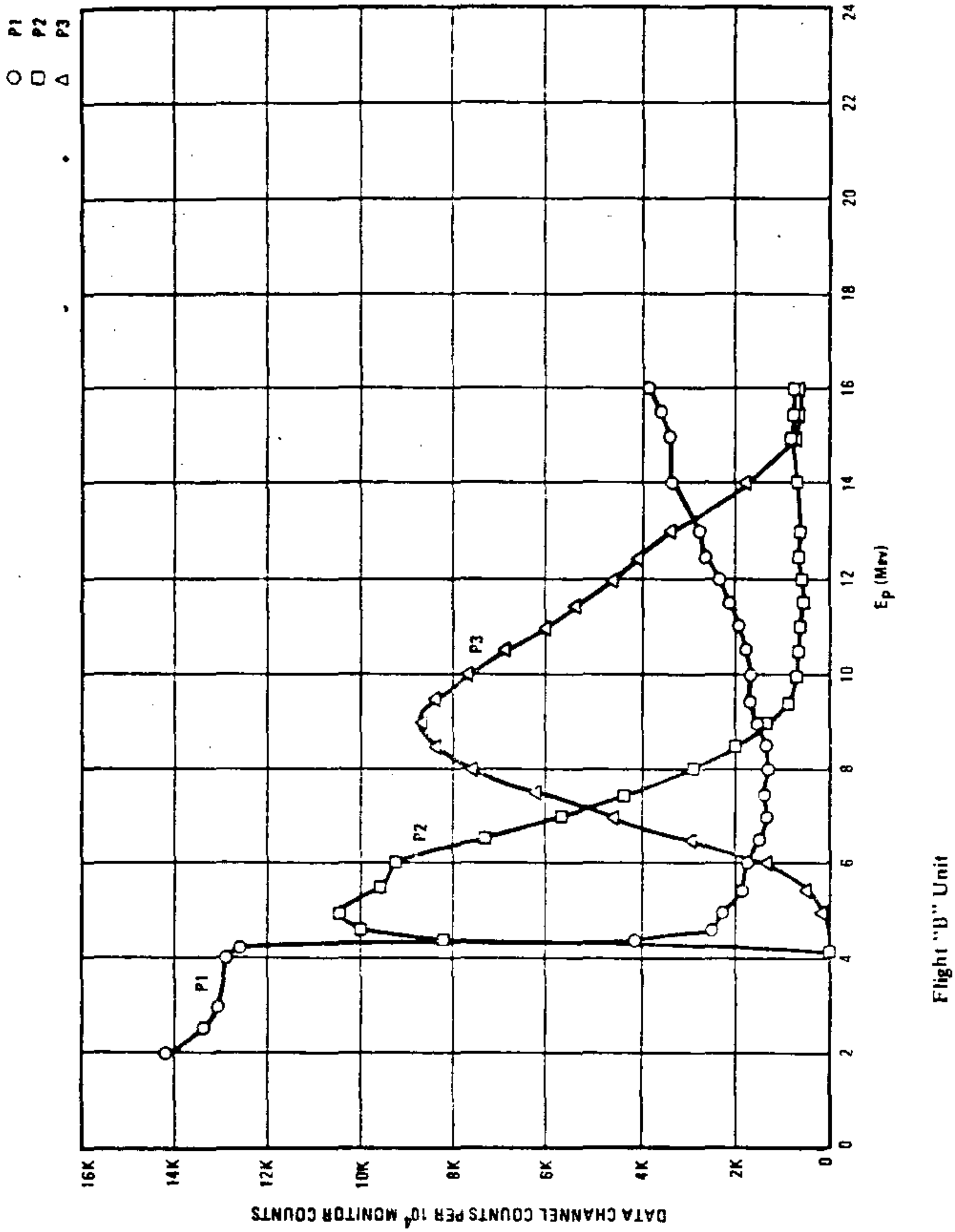

Figure 4.1 "SMS B" Proton Calibration Data (taken directly from Ref. 1.8, Figure 5).

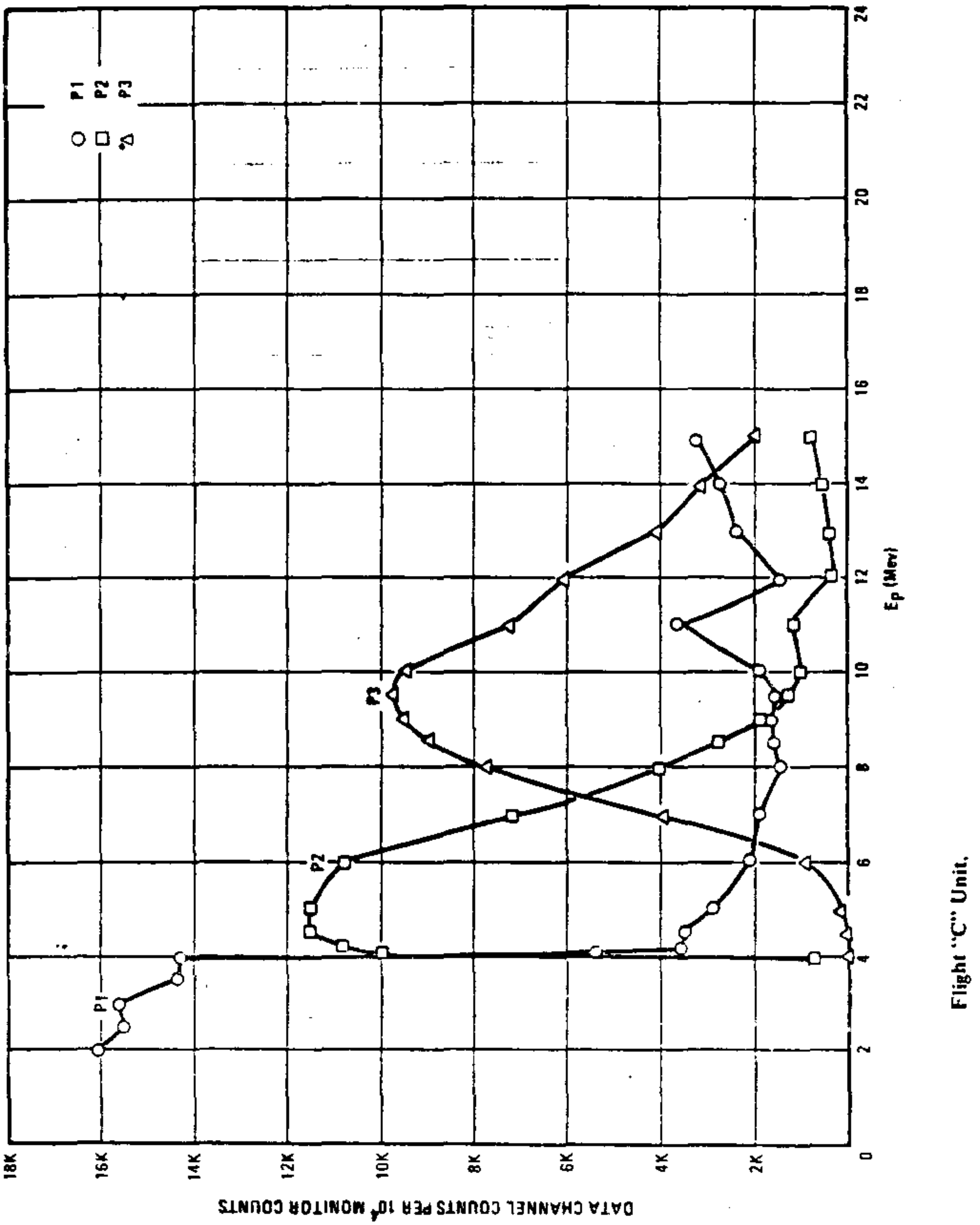

Figure 4.2 "SMS C" Proton Calibration Data (taken directly from Ref. 1.8, Figure 8).

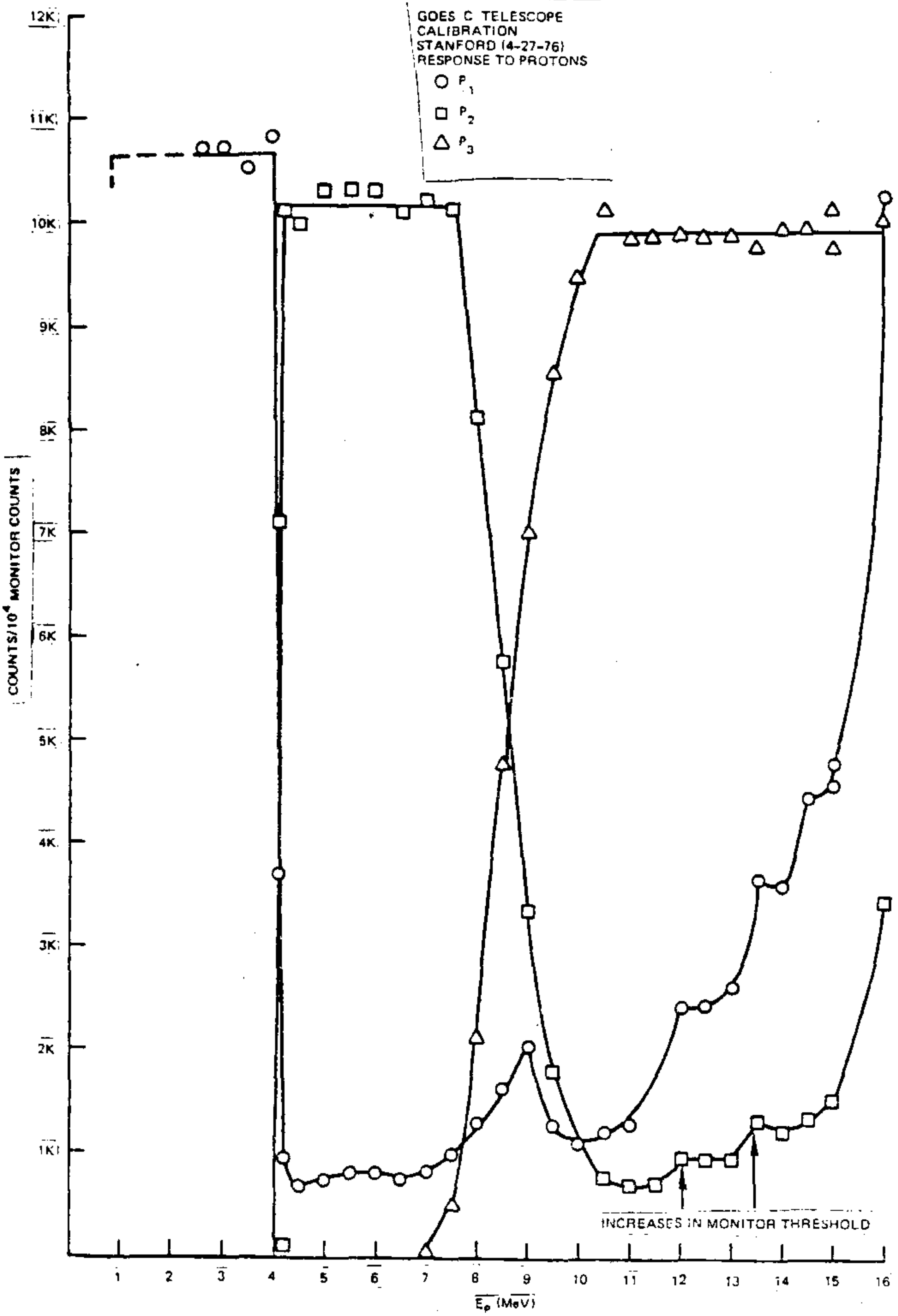

Figure 4.3 GOES C Proton Calibration Data (taken directly from Ref. 1.9, Figure 10).

causes no difficulty in the instrument because the lowest threshold setting (#1, (Table 1.3)) is about 0.3 MeV. However, for GOES C, the level 1 setting was lowered to about 0.15 MeV (Ref. 1.9, p. 5). The energy loss diagram for GOES C (Ref. 1.9, Figure 12) is quite similar to that in Figure 1.2. There it can be seen that lowering #1 to 0.15 causes the energy channel limit to be defined by the coincidence requirement with level 4, rather than level 1 as in the SMS and present Telescopes. From the GOES B and C detector thicknesses and thresholds (Ref. 1.9, p. 5), we calculate that the upper limit of P3 should be about 16 and 13 MeV, respectively, for B and C. Yet, the response curve in Figure 4.3 for GOES C shows no sign of decreasing, even near the ~ 16 MeV maximum proton energy. This, of course, could be the result of experimental uncertainty associated with the monitor detector threshold; or it could be associated with incorrect settings of the energy thresholds. In that context, it should be noted that our calculations (referred to above) of energy loss in front detector vs. energy loss in back detector, near the level 4 threshold, fall very substantially off of the curves given for GOES B and C (Ref. 1.9, Figure 12). In our judgment, if the upper limit value of Channel P3 on GOES B and C is important, some effort should be directed to removing the seeming ambiguities.

In conclusion, the GOES D, E and F Telescope design presented above meets all design specifications, with some significant edge effects problems having been totally eliminated. As a result of the present calibration work the geometrical factors are available, for both the primary and spurious effects, in sufficient detail to allow, for the first time, a detailed analysis of solar particle energy spectra by use of the GOES Telescope data.

5. ACKNOWLEDGEMENTS

The experimental work at Brookhaven National Laboratory was carried out as part of Experiment #188. We are pleased to acknowledge the authorization of time for this experiment by the Program Advisory Committee, whose Chairman was Dr. J. Weneser at the time of this work. Much needed assistance at the Tandem Van de Graaff was provided by Dr. Ott C. Kistner, User Liaison, Mr. George Hummer, and other members of the operating staff, to whom we express sincere appreciation.

The work at the Harvard Cyclotron was carried out with the able assistance of Dr. Robert Schneider, Dr. Andy Kohler, and the other members of the staff.

Mr. Robert Varga and Mr. Dennis Padrick of Hughes Aircraft Company monitored the overall work and participated in data taking at the two accelerator facilities. Their help was very much appreciated.

****

REFERENCES

1.1 Bichsel, H. and C. Tschalaer, A Range-Energy Table for Heavy Particles in Silicon, Nuc. Data A, 3, 343 - 360 (1967).

1.2 Janni, J.F., Calculations of Energy Loss, Range, Pathlength, Straggling, Multiple Scattering, and the Probability of Inelastic Nuclear Collisions for 0.1 To 1,000 - MeV Protons. AFWL-TR-65-150 (1966).

1.3 Hill, C.W., W.B. Ritchie, and K.M. Simpson, Data Compilation and Evaluation of Space Shielding Problems, Vol I, ER7777, N66 - 15586 (1966).

1.4 Hanser, F.A., and B. Sellers, "Measurement of Totally Depleted Silicon Solid State Detector Thickness by X-Ray Attenuation", Rev. Sci. Instrum. 45, 226 - 231 (1974).

1.5 GOES D, E and F PROGRESS REPORT, EPS Tandem Van de Graaff Calibration Work Data Report #1, PANA-GOESC-PR1 (15 August 1978).

1.6 GOES D, E and F PROGRESS REPORT, EPS Tandem Van de Graaff Calibration Work, Data Report #2, PANA-GOESC-PR2 (25 September 1978).

1.7 Young, A.M., EPS Development Test Summary, Philco - Ford Corp., 1W99 - 1 - 35 (13 October 1972).

1.8 Rinehart, M.C., SMS - A, B, C EPS Calibration, Philco - Ford Corp., 3G4600 - 74 - 079, Rev A, SMS - PCC -6252 (29 March 1974).

1.9 Nuclear Calibrations for the GOES B & C EPS, 3G9300 - 76 - 094, GOES -PCC-549 (12 August 1976).

2.1 Seltzer, S.M., and M.J. Berger, "Energy-Loss Straggling of Protons and Mesons: Tabulation of the Vavilov Distribution", pp. 187 - 203 in Studies in Penetration of Charged Particles in Matter, Nat'l Acad. Sci. Publ. #1133, Washington, D.C. (1964).

2.2 Abramowitz, M., and I.A. Stegun, Handbook of Mathematical Functions, NBS Publ., Appl. Math. Series 55 (1964).

2.3 Bichsel, H., Straggling and Particle Identification in Silicon Detectors, Nucl. Instr. Meth. 78, 277 - 284 (1970).

2.4 Hanser, F.A., B. Sellers, and P.R. Morel, A Proton - Alpha Particle Detector for Use in Satellites, AFCRL-TR-73-0144, AD 760 147 (1973).